Università degli Studi di Torino

FACOLTÀ DI SCIENZE MATEMATICHE, FISICHE E NATURALI

Corso di Laurea Magistrale in Fisica

Tesi di laurea magistrale

Measurement of the relative production cross section of $\chi_{b2}(1P)$ and $\chi_{b1}(1P)$ in proton-proton collisions with the CMS experiment at LHC

Misura della sezione d'urto di produzione relativa di $\chi_{b2}(1P)$ e $\chi_{b1}(1P)$ in collisioni protone-protone con il detector CMS a LHC

Candidato:
Giulio Dujany
Matricola 703648

Relatore:
Prof. Ernesto Migliore

Correlatore:
Prof. Stefano Argirò

Anno Accademico 2012–2013

CONTENTS

LIST OF FIGURES

LIST OF TABLES

ABSTRACT

In this thesis is presented the first measurement of the prompt production cross section ratio of the $\chi_{b2}(1P)$ and $\chi_{b1}(1P)$ bottomonium states performed by detecting their radiative decays $\chi_{b2,1} \rightarrow \Upsilon(1S) + \gamma$ in CMS. The photon is measured through pair conversion in the tracker, which allows the two states to be resolved with good separation. The measurement was performed in the kinematical region $|y(\Upsilon)| < 1.25$, $|\eta(\gamma)| < 1.0$, $7.0\ GeV < p_T(\Upsilon) < 40.0\ GeV$. 20.7 fb^{-1} of data from proton-proton collisions at $\sqrt{s}$=8 TeV collected in 2012 were analyzed.

SOMMARIO

In questa tesi è presentata la prima misura del rapporto tra le sezioni d'urto di produzione di $\chi_{b2}(1P)$ e $\chi_{b1}(1P)$. Il decadimento radiativo $\chi_{b2,1} \rightarrow \Upsilon(1S) + \gamma$ è stato analizzato e, per ottenere una risoluzione sufficiente per distinguere i due stati, il fotone è rivelato a partire dalle conversioni nel tracker. La misura è stata eseguita nella regone cinematica $|y(\Upsilon)| < 1.25$, $|\eta(\gamma)| < 1.0$, $7.0\ GeV < p_T(\Upsilon) < 40.0\ GeV$. Sono stati analizzati 20.7 fb^{-1} di dati da collisini protone-protone a $\sqrt{s}$=8 TeV raccolti nel 2012 dall'esperimento CMS.

On fait la science avec des faits comme une maison avec des pierres mais une accumulation de faits n'est pas plus une science qu'un tas de pierres n'est une maison.

— Henri Poincaré

ACKNOWLEDGMENTS

Many are the people to whom I am indebted and who made this thesis possible, from my family and my friends to the CMS experiment, expecially the Torino's group. It is a great pleasure to thank in particular my supervisors Ernesto Migliore and Stefano Argirò for their invaluable assistance and guidance, my sincere thanks also to Alessandro Degano for the support, and to Hermine Wöhri, Carlos Lourenço and Valentin Knünz for the useful suggestions and discussions.

INTRODUCTION

Quarkonium, a bound state formed by an heavy quark and its antiquark, is an exceptional system to prove our understanding of quantum chromodynamics. In its physics different energy scales play an important role and both perturbative and non perturbative effects must be taken into account. Although most of its features are well described by phenomenological models, as the potential models, or by the more theoretical grounded tools of effective field theories, as non relativistic quantum chromodynamics, open questions still remain. Its production mechanism in hadron colliders, for example, is described in various theoretical frameworks. Precision measurement are then needed to discriminate between models and to constrain their free parameters.

In this thesis is presented the first world measurement of the production cross section ratio:

$$\sigma(pp \to \chi_{b2}(1P) + X)/\sigma(pp \to \chi_{b1}(1P) + X).$$

in four bins of $p_T(\Upsilon)$. Bottomonium states are reconstructed by detecting their radiative decays $\chi_{b2,1} \to \Upsilon(1S) + \gamma$ in the Compact Muon Solenoid (CMS) experiment at the Large Hadron Collider (LHC). The photon is measured through pair conversion in the CMS tracker, which allows the two states to be resolved with good separation.

The high luminosity delivered by LHC in 2012 and the good resolution on the photon energy allowed by the tracker were essential for performing this measurement.

The first chapter briefly summarizes the theoretical framework used to describe the quarkonia states. Various theories to explain its production in hadron colliders are presented along with their prediction to the ratio which will be measured in this thesis. A pedagogical description of relativistic quantum chromodynamics is also given. Finally a brief summary of the properties of χ_b state is presented.

The second chapter is devoted to the description of the Large Hadron Collider and, in particular, of the Compact Muon Solenoid experiment. Its sub-detectors are described highlighting the characteristics that made this analysis possible. Some details are also given about the software framework and the data storage model used in CMS.

The third chapter presents the measurement describing all the details of the analysis. The datasets used are listed and the simulation strategy is depicted. The event selection is then defined along with the strategy to discriminate between signal and background. Various sources of possible systematics uncertainties are examined.

1 THEORY OVERVIEW

The present chapter gives a brief introduction to basic concepts of quarkonium physics and the theoretical frameworks used to describe its production. More attention is given to non relativistic quantum chromodynamics, by now the theory most successful phenomenologically successful and theoretically sound we have to describe quarkonium states. Finally a brief overview of the theoretical predictions of $\sigma(\chi_{b2})/\sigma(\chi_{b1})$ is given.

In the following $\hbar = c = 1$.

1.1 QUARKONIUM

Heavy quarkonium consists of a meson containing a heavy quark and its antiquark.The *charm*, the *beauty* (or *bottom*) and the *top* quark are considered heavy quarks because their mass is bigger than Λ_{QCD} ($\sim 200\,\text{MeV}$), the scale at which the perturbative expansion in powers of α_s would diverge so that prediction based on pQCD (perturbative Quantum Chromodynamics) can not be made. Actually only quarkonia formed by charm (*charmonium*) or bottom (*bottomonium*) are observed as the top quark has a very short life time and decays before bound states can be formed.

The typical velocity of valence quarks in quarkonium is non relativistic ($v^2 \sim 1/3$ for charmonium and $v^2 \sim 1/9$ for bottomonium). Quarkonium can thus be considered to a first approximation as a non relativistic quantum system and thus be described by the following quantum numbers:

n the radial quantum number,

L the eigenvalue of radial angular momentum,

S the eigenvalue of the spin,

J the eigenvalue of the total angular momentum.

A quarkonium state can thus be specified by its spectroscopic notation $\left|^{2S+1}L_J\right\rangle$. The spectrum of bottomonium is shown in figure 1.1.

The first excited state above the ground state for $c\bar{c}$ is the J/ψ ($m_{J/\psi} = 3.1$ GeV, $\Gamma_{J/\psi} = 91$ keV), while for $b\bar{b}$ mesons is the

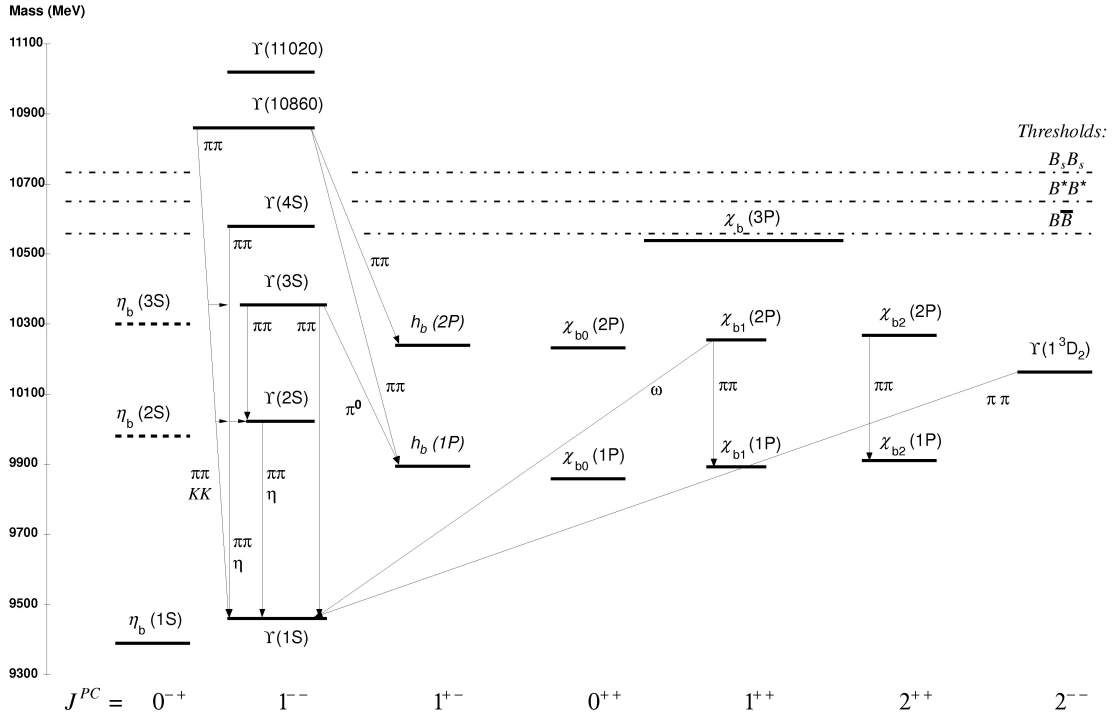

Figure 1.1.: Bottomonium spectroscopy diagram

Υ ($m_\Upsilon = 9.46$ GeV, $\Gamma_\Upsilon = 54$ keV). The lower-mass states of heavy quarkonium resonances are relatively stable particles: as their mass is below the threshold for open heavy flavored meson production , their decay modes are either electromagnetic or OZI-suppressed; their width ranges from a few dozens keV to a few dozens MeV.

Potential model

The spectroscopy of quarkonia is phenomenological described by assuming that the $Q\bar{Q}$ pair is subjected to the *Cornell potential*:

$$V(r) = -\frac{4}{3}\frac{\alpha_s(R)}{R} + \kappa^2 R \tag{1.1}$$

where $4/3$ is a color factor, α_s is the strong coupling constant, R is the distance between the two quarks and $\kappa \simeq 450$ MeV. This potential consists of a Coulomb-like term, accounting for the gluon-exchange between the two quarks, and a confining term parameterizing the non-perturbative effects. The results obtained by solving the non relativistic Schrödinger equation with the potential (1.1) with ad-hoc values of the parameters are in good agreement with the observed spectra.

Energy Scales

Quarkonium is a very challenging system to study as there are a number of different energy scales that play a role in its physics.

- M, the mass of the quarkonium state, sets the total energy scale for annihilation decays and the scale of the kinematic threshold for quarkonium production.
- Mv is the typical momentum of the valence quarks, it is also the inverse of the length scale for the size of the quarkonium states.
- Mv^2 is the typical kinetic energy, it is the scale of the splittings between radial excitations and between orbital-angular-momentum excitations in the quarkonium spectrum.

An estimate of these scales [22] can be found in table 1.1.

Table 1.1.: Quarkonium energy scales.

	$c\bar{c}$	$b\bar{b}$
M [GeV]	1.5	4.7
Mv [GeV]	0.9	1.5
Mv^2 [GeV]	0.5	0.5

Another important energy scale in quarkonium physics is Λ_{QCD}, the scale of nonperturbative effects involving gluons and light quarks. To clarify its relation with the typical scales of quarkonium two limiting cases can be considered: Λ_{QCD}

1. The heavy quark mass is large enough so that the Cornell potential (1.1) is dominated by the Coulomb-like term. The size of the bound state is then determined by a balance between the kinetic energy and the potential energy:

$$Mv^2 \sim \frac{4}{3}\frac{\alpha_s(r)}{r} \tag{1.2}$$

The size of the bound state (R) is comparable to the inverse of the typical momentum $R \sim 1/(Mv)$, making this substitution in 1.2:

$$v \sim \alpha_s(Mv)$$

solving this equation, v can be expressed as a function of M. For example if M was sufficiently large, the resulting value of Mv^2 would be much greater than Λ_{QCD}.

2. The heavy mass is small enough that the Cornell potential (1.1) is dominated by the linear term. The balance between kinetic and potential energy requires

$$Mv^2 \sim \kappa^2 R \tag{1.3}$$

setting $R \sim 1/(Mv)$, it is clear that $\kappa \sim Mv^{3/2}$. As the linear term parameterize the non-perturbative effects, κ is independent of M,it must be proportional to Λ_{QCD}. Identifying κ with Λ_{QCD}:

$$Mv^2 < \Lambda_{QCD} < Mv.$$

the comparison of potential models with data has shown that κ does not depend on the mass of the quarkonium state

Considering an intermediate case where both the Coulomb-like and the linear term are important, then (1.2) and (1.3) would be satisfied simultaneously so that

$$Mv^2 < \Lambda_{QCD} < Mv \ll M.$$

In quarkonium physics thus both perturbative and non-perturbative QCD play a role. This can be better understood from the values of α_s at the various characteristic quarkonium energy scales summarized in table 1.2

Table 1.2.: Value of the QCD coupling constant at the characteristic momentum scales for heavy quarkonium.

	$c\bar{c}$	$b\bar{b}$
α_s (M)	0.35	0.22
α_s (Mv)	0.52	0.35
α_s (Mv^2)	$\gg 1$	$\gg 1$

Finally for quarkonium production in hadron colliders the intrinsic scale of the hard scattering must also be considered. The hard-scattering scale p is usually set by a large momentum transfer between the partons in the production process and it is taken to be of the order of the quarkonium p_T.

1.2 QUARKONIUM PRODUCTION

The mechanism of quarkonium production at hadron colliders is still an open research field.

Partons involved

Electromagnetic production

The hypothesis of electromagnetic production similar to the Drell Yan process has been ruled out in fixed target experiments: the cross section would be proportional to the square of the charge of the annihilating quark and, for example, the ratio of cross sections

$$\frac{\sigma(\pi^- N \to q\bar{q}X)}{\sigma(\pi^+ N \to q\bar{q}X)} = \frac{Q(\bar{u})^2}{Q(\bar{d})^2} = \frac{(2/3)^2}{(1/3)^2} = 4$$

which is not observed.

Likewise if $q\bar{q}$ annihilation into a gluon (figure 1.2a) was the main process this would lead to a suppression of a factor $5-10$ in proton-proton collisions with respect to proton-antiproton ones. The suppression observed in experiments is much smaller so this cannot be the main process.

Quarkonia production must thus be dominated by gluon fusion or gluon fragmentation (figures 1.2b and 1.2c).

Factorization

As already mentioned in section 1.1 quarkonium physics is characterized by both perturbative and non-perturbative aspects. For what concerns its production, intuitively it could be understood in terms of two distinct steps:

1. the production of the $Q\overline{Q}$ pair which occur at the scale p (a large momentum transferred in the production process) and can be described perturbatively in expansions of $\alpha_s(p)$,

2. the evolution of the $Q\overline{Q}$ pair into the quarkonium which involve smaller dynamical scales Mv and mv^2 and thus a non-perturbative physics.

The term *short distance* is often used to refer to the momentum scale p while the term *long distance* refers to typical hadronic momentum scales such as Mv, Mv^2 or Λ_{QCD}.

In order to show that short distance perturbative effects at the scale p can be separated from the long distance non-perturbative dynamics a *factorization theorem* must be provided. It must be shown that an amplitude or a cross section can be expressed as a sum of products of infrared safe short distance coefficients with well defined operator matrix elements. Short distance coefficients will be perturbatively calculable while the operator matrix elements will contain all the long distance, non-perturbative physics and will be determined phenomenologically or through

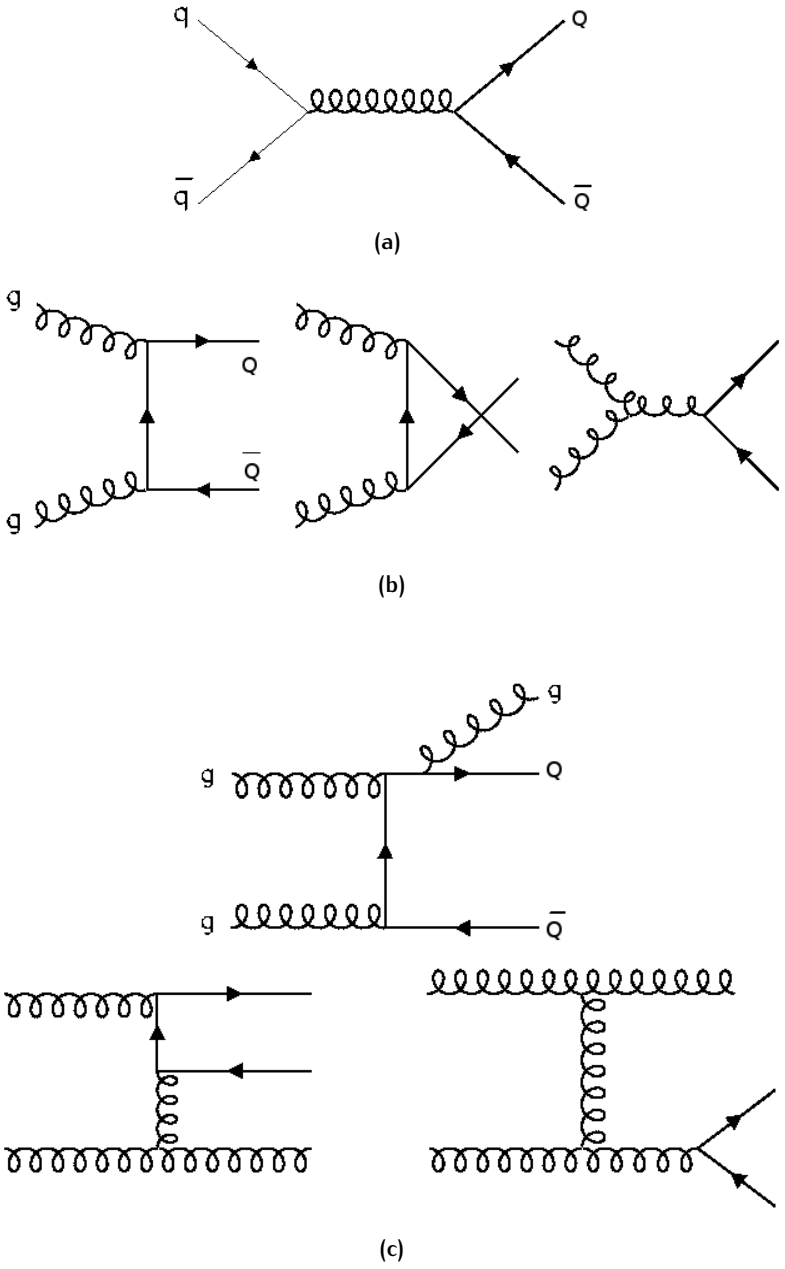

Figure 1.2.: Main Feynman diagrams contributing to quarkonium production.

lattice simulations. If it could be demonstrated that the long distance elements are universal (i. e. process independent) the factorization formula would yield much greater predictive power.

Various models have been proposed that achieve this factorization, the most notable among these are the *color evaporation model* (CEM), the *color singlet model* (CSM) and the *nonrelativistic QCD* (NRQCD).

Colour Evaporation Model (CEM)

In this model it is assumed that each $Q\overline{Q}$ pair, whose mass is less than the threshold for producing a pair of open-flavor heavy mesons, evolves into a quarkonium state. The probability of a produced $Q\overline{Q}$ pair to evolve into a certain quarkonium state H is given by a constant F_H which is independent from the process and the energy-momentum of the $Q\overline{Q}$ pair. The $Q\overline{Q}$ is assumed to neutralize its color by interaction with the collision-induced colour field by colour evaporation so that F_H is also independent from $Q\overline{Q}$ quantum numbers. The production cross section of a quarkonium H is thus the fraction F_H of the production cross section of the $Q\overline{Q}$ pair:

$$\sigma_H = F_H \cdot \sigma_{Q\overline{Q}}.$$

The $Q\overline{Q}$ production cross section can be calculated perturbatively while F_H is the only parameter to be fixed by comparison with the measured total cross section for the production of the quarkonium state H. The CEM can than predict with no additional free parameters, for example, the momentum distribution of the quarkonium production rate.

The CEM predictions provide a rough description of CDF data for J/ψ, $\psi(2S)$ and χ_c production with a poorer agreement with data with respect to NRQCD. Moreover its most basic prediction is that the ratio of the cross sections of any two quarkonium states should be independent from the process and the kinematic region; variations of these ratios have however been observed.

Color Singlet Model (CSM)

The color-singlet model (CSM) was first proposed shortly after the discovery of the J/ψ. The main concept of the CSM is that, in order to produce a quarkonium state, the $Q\overline{Q}$ pair must be generated with the quarkonium quantum numbers; in particular the pair has to be produced in a color-singlet state. The production rate of a quarkonium state is related to the absolute value of the

color-singlet $Q\bar{Q}$ wave function and its derivative[1] evaluated at zero $Q\bar{Q}$ separation. These quantities can be extracted from decay rates leaving no free parameters in predicting the production cross section.

The CSM was successful in predicting quarkonium production rates at relatively low energies. At leading order (LO) however it underestimated the J/ψ and $\psi(2S)$ production cross section at Tevatron by a factor 50 (see figure 1.3).

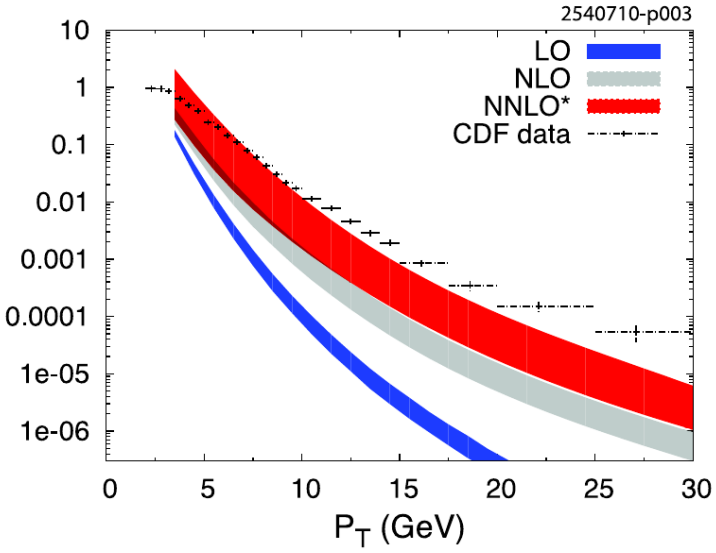

Figure 1.3.: Comparison between CSM prediction for the $\psi(2S)$ cross section at LO, NLO and NNLO* accuracy as a function of $p_T(\psi(2S))$ at Tevatron at $\sqrt{s} = 1.96\,\text{TeV}$

Considering next-to-leading order (NLO) and next-to-next-to-leading order (NNLO) corrections in α_s, very large terms appear which improve the CSM agreement with data also at large p_T. It is however unclear if the perturbative expansion in α_s converges.

Non Relativistic QCD (NRQCD)

The NRQCD factorization approach is the most theoretically grounded and the most phenomenologically successful mechanism to describe quarkonium production. NRQCD is an *effective field theory* of QCD which reproduces full QCD results at momentum scales less than Mv. The physics involving higher momentum scales is parameterized in the *short distance coefficients* of the operators that appear in the NRQCD Lagrangian. A short introduction to this theory is given in the next section.

1 More precisely its L-th derivative.

1.3 NRQCD

1.3.1 Effective field theories

In physical problems often different energy scales widely separated are involved. This allows, when studying a low energy problem, to neglect the details of the hight energy physics parameterizing the global effects in a small number of parameters.

Let us consider, in general, a quantum field theory for the field ϕ defined by the Feynman path integral

$$\int \mathcal{D}\phi \; e^{iS} \qquad \text{where} \qquad S = \int d^D x \; \mathcal{L}. \tag{1.4}$$

Considering a energy scale Λ, it is possible to separate the high energy (short distance) from the low energy (long distance) components of the field ϕ:

$$\phi = \phi_L + \phi_H$$

where, Fourier-transforming the field ϕ

$$\phi(x) = \int \frac{d^{D-1}p}{2\omega(2\pi)^{D-1}} \left[a(\vec{p}) e^{i(\vec{p}\cdot\vec{x}-\omega t)} + a^\dagger(\vec{p}) e^{-i(\vec{p}\cdot\vec{x}-\omega t)} \right]$$

we have defined

$$\phi_L : \omega < \Lambda$$
$$\phi_H : \omega > \Lambda$$

so that (1.4) becomes

$$\int \mathcal{D}\phi \; e^{iS(\phi)} = \int \mathcal{D}\phi_L \mathcal{D}\phi_H \; e^{iS(\phi_L,\phi_H)} = \int \mathcal{D}\phi_L \; e^{iS_\Lambda(\phi_L)}$$

where

$$e^{iS_\Lambda(\phi_L)} = \int \mathcal{D}\phi_H \; e^{iS(\phi_L,\phi_H)}.$$

Evaluating the path integral over energies greater than Λ we obtain an effective action S_Λ called *Wilsonian effective action* that can be rewritten as

$$S_\Lambda = \int d^D x \; \mathcal{L}_\Lambda = \int d^D x \; \sum_i g_i \mathcal{O}_i. \tag{1.5}$$

where the effective Lagrangian has been expanded in a sum, in general infinite, over all the local operators compatibles with the symmetries of the system.

In practice the integral over the high energies needed to obtain the effective Lagrangian is not performed explicitely. The most general combination of operators O_i compatible with the symmetries of the system must be written and the coupling constants g_i are free parameters to be determined from the experimental data.

At this point no approximation has been made and the theory $\mathcal{L}_\Lambda$ is perfectly equivalent to $\mathcal{L}$. However it has in general an infinite number of free parameters to be determined from experiment. By dimensional analysis however it is possible to identify the leading terms in the expansion (1.5).

Dimension

Defining $[x]$ the dimension (in energy) of a given quantity x, it is easy to see that $[S] = 1$, $[d^D x] = -D$ and $[\mathcal{L}] = D$. As a consequence each term in the expansion (1.5) has the same dimension $[g_i \mathcal{O}_i] = D$. If d_i is the dimension of the operator $\mathcal{O}_i$ ($[\mathcal{O}_i] = d_i$) then the dimension of the coupling constant must be $[g_i] = D - d_i$. As the effective field theory is defined by the scale Λ, and g_i is an energy to the power $D - d_i$, it is possible to rewrite g_i as

$$g_i = \lambda_i \Lambda^{D-d_i} = \frac{\lambda_i}{\Lambda^{d_i - D}}$$

where λ_i is dimensionless quantity expected to be $O(1)$ as Λ is the typical scale of the system.

Then

$$\mathcal{L}_\Lambda = \sum_i \frac{\lambda_i}{\Lambda^{d_i - D}} \mathcal{O}_i$$

and (1.5) becomes:

$$S_\Lambda = \int d^D x \, \mathcal{L}_\Lambda = \int d^D x \, \sum_i \frac{\lambda_i}{\Lambda^{d_i - D}} \mathcal{O}_i .$$

Studying a process at the energy E it is possible to estimate the magnitude of each term in the expansion

$$\int d^D x \, \mathcal{O}_i \sim E^{d_i - D}$$

so that the i-th term will be approximately

$$\lambda_i \left(\frac{E}{\Lambda} \right)^{d_i - D} .$$

If $E \ll \Lambda$, and $d_i - D > 0$ the magnitude of the i-th term will be negligible; at the contrary if $d_i - D < 0$ it will be one of the leading term of the expansion.

There are three cases:

RELEVANT COUPLING $d_i < D$, the magnitude of this term grows if the energy E decreases.

MARGINAL COUPLING $d_i = D$, the magnitude of this term is independent from the value of the energy E.

IRRELEVANT COUPLING $d_i > D$, the magnitude of this term falls if the energy E decreases.

To describe a system at an energy scale $E \ll \Lambda$, we can approximate the expansion (1.5) keeping only the relevant and marginal couplings. Irrelevant couplings will provide higher order correction needed in precision measurements.

There are two ways to determine the values of the coupling constants g_i: *matching conditions*

1. Compute them from the full theory constraining that the effective theory and the full theory give the same results in a certain number of processes.

2. Evaluate them from experiment.

1.3.2 Relativistic Effects

The general prescriptions described in the previous section can be applied to the QCD Lagrangian to obtain the non relativistic QCD. The original QCD Lagrangian with the heavy quark is

$$\mathcal{L}_{QCD} = \mathcal{L}_{light} + \bar{\Psi}(i\gamma^\mu D_\mu - m_Q)\Psi \tag{1.6}$$

where $\mathcal{L}_{light}$ is the Lagrangian that describes gluon and light quarks and the mass parameter m_Q can be identified with M. Now we want to obtain an effective Lagrangian using a cutoff $Mv \ll \Lambda \ll M$. In the resulting theory the effects at energy scales higher than Λ will be reproduced by local interactions. For example a virtual state that includes a gluon with relativistic momentum of order M is off its mass-shell by an amount of order M. Thus, by the uncertainty principle, has a lifetime of order $1/M$ and can propagate only over distances of order $1/M$ which is point-like compared to $1/(Mv)$.

Moreover in this theory the heavy quarks are not relativistic and will therefore better described by two two-components Pauli fields ψ and χ rather than by a Dirac field. In the Dirac representation of gamma matrices:

$$\Psi = \begin{pmatrix} \psi \\ \chi \end{pmatrix}$$

To remove off diagonal terms that couples ψ from χ a unitary transformation is needed that diagonalizes the Lagrangian at the desired order. Such trasformation is known as Wouthuysen-Tani transformation and at leading order is

$$\Psi \to \exp -i\vec{\gamma}\cdot\vec{D}/2m_Q\Psi$$

so that the heavy quark term in the Lagrangian (1.6) can be approximated by

$$\begin{pmatrix}\psi & \chi\end{pmatrix}^\dagger \begin{pmatrix}-m_Q + iD_0 + \vec{D}^2/2m_Q & 0 \\ 0 & m_Q + iD_0 - \vec{D}^2/2m_Q\end{pmatrix}\begin{pmatrix}\psi \\ \chi\end{pmatrix}$$

where if $\vec{D}$ scales like Mv, the neglected terms scale at least like Mv^4. To apply a Λ cutoff to $\mathcal{L}_{\text{light}}$ is more difficult because it would require to separate high energy modes from low energy modes in gluon and light quarks fields. Luckily it is not required as the effective field theory prescription is to write the more general Lagrangian compatible with the symmetries of the studied system.

1.3.3 Symmetries

The fields described by NRQCD are the heavy quark and antiquark fields ψ and χ, the $SU(3)$ gauge field A_μ and the Dirac fields of the light quarks. The symmetries of NRQCD are:

$SU(3)$ **GAUGE SYMMETRY** the gluon field enters into the effective Lagrangian only through the gauge-covariant derivatives D_0 and $\vec{D}$ and the QCD field strengths $\vec{E}$ and $\vec{B}$.

ROTATIONAL SYMMETRY being a non relativistic description it breaks the Lorentz symmetry keeping only its rotational subgroup.

CHARGE CONJUGATION AND PARITY the charge conjugation transformations of the heavy quark and antiquark fields are:

$$\psi \to i(\chi^\dagger\sigma_2)^t, \qquad \chi \to -i(\psi^\dagger\sigma_2)^t$$

and their parity transformations are:

$$\psi(t,\vec{r}) \to \psi(t,-\vec{r}), \qquad \chi(t,\vec{r}) \to -\chi(t,-\vec{r})$$

HEAVY-QUARK PHASE SYMMETRY it guarantees the separate conservation of quarks and antiquarks. Its action on the fields is:

$$\psi \to e^{i\alpha}\psi, \qquad \chi \to e^{i\beta}\chi$$

1.3.4 Effective field theory

The most general Lagrangian consistent with the symmetries outlined above is:

$$\mathcal{L}_{\text{NRQCD}} = \mathcal{L}_{\text{light}} + \psi^\dagger \left(iD_0 + \frac{\vec{D}^2}{2M} \right) \psi + \chi^\dagger \left(iD_0 - \frac{\vec{D}^2}{2M} \right) \chi + \delta\mathcal{L} \tag{1.7}$$

The desired level of accuracy is specified by the order in v with which the quarkonium energy levels must be reproduced. By setting $\delta\mathcal{L} = 0$, the Lagrangian (1.7) can be used to calculate the energy levels up to errors of order Mv^4. In this approximation radial and orbital-angular-momentum energy splittings are reproduced (i. e. between Υ (1S) and Υ (2S) and between Υ (1S) and χ_b(1P)), which are of order Mv^2 but not spin splittings (i. e. between η_b and Υ (1S)) which scale like Mv^4.

To increase the precision leaving errors of order Mv^6, $\delta\mathcal{L}$ must be set to:

$$\begin{aligned}\delta\mathcal{L} =& \frac{c_1}{8M^3}\psi^\dagger(\vec{D}^2)^2\psi + \frac{c_2}{8M^2}\psi^\dagger(\vec{D}\cdot g\vec{E} - g\vec{E}\cdot\vec{D})\psi + \\ &+ \frac{c_3}{8M^2}\psi^\dagger(i\vec{D}\times g\vec{E} - g\vec{E}\times i\vec{D})\cdot\vec{\sigma}\psi + \frac{c_4}{2M}\psi^\dagger(g\vec{B}\cdot\vec{\sigma})\psi + \\ &+ \text{charge coniugate terms}\end{aligned}$$

which breaks the spin symmetry. A redefinition of the fields ψ and χ has been used to eliminate all occurrences of D_0 in $\delta\mathcal{L}$ except in the combination $[D_0, \vec{D}] = ig\vec{E}$. Due to these redefinitions of the fields, NRQCD will not agree with QCD at the level of Green's functions but only for predictions on on-shell physical quantities.

1.3.5 Velocity scaling rules

The relative importance of the terms in NRQCD is not only expressed in negative powers of Λ as in the general case but, being a non-relativistic approximation, also the powers of v must be taken into account. In this case simple dimensional analysis is not sufficient to deduce the scaling relations of the various terms of the NRQCD Lagrangian but the knowledge of basic qualitative features of quarkonium is also required.

Heavy quark fields

The scaling of ψ can be derived knowing that the expectation value of the number operator $\int d^3x\, \psi^\dagger\psi$ in a quarkonium state $|H\rangle$ is close to one:

$$\left\langle H \left| \int d^3x\, \psi^\dagger\psi \right| H \right\rangle \approx 1$$

with the quarkonium state normalized to 1 $\left(\langle H | H \rangle = 1\right)$. Knowing that the quarkonium state is localized within a region $1/(Mv)^3$, it can be concluded that ψ scales like $(Mv)^{3/2}$. The same stands for χ.

Gauge-covariant derivative

The scaling rule of the gauge-covariant derivative can be deduced knowing that the expectation value of the kinetic energy term of the NRQCD Hamiltonian scales like Mv^2:

$$\left\langle H \left| \int d^3x \, \psi^\dagger \left(\frac{\vec{D}^2}{2M} \right) \psi \right| H \right\rangle \approx Mv^2$$

so that $\vec{D}$ must scale like Mv; from the field equations for ψ:

$$\left(iD_0 - \frac{\vec{D}^2}{2M} \right) \psi = 0$$

follows then immediately that D_0 scales like Mv^2.

These and the other scaling rules derived in [22] are summarized in table 1.3

Table 1.3.: Estimates of the magnitudes of NRQCD operators for matrix elements between heavy-quarkonium states.

Operator	Estimate
ψ	$(Mv)^{3/2}$
χ	$(Mv)^{3/2}$
D_0 (acting on ψ or χ)	Mv^2
$\vec{D}$	Mv
$g\vec{E}$	M^2v^3
$g\vec{B}$	M^2v^4
gA_0 (in Coulomb gauge)	Mv^2
$g\vec{A}$ (in Coulomb gauge)	Mv^3

1.3.6 Coulomb gauge

The Coulomb gauge is defined by $\vec{\nabla} \cdot \vec{A} = 0$[2]. This is the natural gauge to describe the quarkonium as it is a physical gauge (i. e. it does not contain negative norm states) and avoid delayed effects present in the covariant gauges but not needed in a non

2 in this section the usual notation for electromagnetic fields will be used for cromo-electric ($\vec{E}$) and cromo-magnetic ($\vec{B}$) fields and A_μ will indicate the SU(3) color gauge fields

relativistic theory. In this gauge A_0 does not propagate and dynamical gluons are created and destroyed by the vector potential $\vec{A}$. In this gauge the Lagrangian (1.7) can be reorganized in an expansion in powers of v. Rescaling the space-time coordinates, and all the fields by their scaling factors[3] the powers of v can be made explicit. The terms $O(1)$ after that rescaling are:

$$\mathcal{L}_0 = \mathcal{L}_{\text{light}} + \psi^\dagger \left(i\partial_0 - gA_0 + \frac{\vec{\nabla}^2}{2M} \right) \psi + \chi^\dagger \left(i\partial_0 - gA_0 - \frac{\vec{\nabla}^2}{2M} \right) \chi, \tag{1.8}$$

and finally the terms $O(v)$:

$$\begin{aligned} \mathcal{L}_1 = & -\frac{1}{M}\psi^\dagger(ig\vec{A}\cdot\vec{\nabla})\psi + \frac{c_4}{2M}\psi^\dagger(\vec{\nabla}\times g\vec{A})\cdot\vec{\sigma}\,\psi \\ & + \text{ charge conjugate terms,} \end{aligned} \tag{1.9}$$

the terms $O(v^2)$:

$$\begin{aligned} \mathcal{L}_2 = & -\frac{1}{2M}\psi^\dagger(g\vec{A})^2\psi + \frac{c_1}{8M^3}\psi^\dagger(\vec{\nabla}^2)^2\psi \\ & + \frac{c_2}{8M^2}\psi^\dagger(-\vec{\nabla}^2 gA_0)\psi - \frac{c_3}{4M^2}\psi^\dagger(\vec{\nabla} gA_0)\times\vec{\nabla}\cdot\vec{\sigma}\,\psi \\ & + \frac{c_4}{2M}\psi^\dagger(ig\vec{A}\times g\vec{A})\cdot\vec{\sigma}\,\psi + \text{ charge conjugate terms.} \end{aligned} \tag{1.10}$$

1.3.7 Fock state expansion

Quarkonium state can represented, as a first approximation, as a $Q\overline{Q}$ bound state, a color singlet as represented in the CEM. However in NRQCD the color singlet is only the main term of a Fock structure. There is a non null probability that quarkonium contains additional gluons or pairs of light quark-antiquark. To estimate the probability of the quarkonium state to be in one of these states the velocity scaling rules can be applied [24].

The terms in (1.8) do not couple the heavy quarks fields with the gauge field. The first terms which do so are in (1.9).

The term $\psi^\dagger(ig\vec{A}\cdot\vec{\nabla})\psi$ produces an *electric transition* (E1) from $\left|Q\overline{Q}\right\rangle$ to $\left|Q\overline{Q}\gamma\right\rangle$ with angular momentum quantum numbers which

3 The transformations are:

$$\begin{aligned} r &\to r\cdot(Mv) & t &\to t\cdot(Mv^2) \\ \psi &\to \psi\cdot(Mv)^{-3/2} & \chi &\to \chi\cdot(Mv)^{-3/2} \\ A_0 &\to A_0/(Mv^{3/2}) & \vec{A} &\to \vec{A}/(Mv^{3/2}) \end{aligned}$$

satisfy the selection rules $\Delta L = \pm 1$ and $\Delta S = 0$. Its probability is of order v^2

The term $\psi^\dagger(\vec{\nabla} \times g\vec{A}) \cdot \vec{\sigma}\psi$ produces a *magnetic transition* (M1) from $\left|Q\overline{Q}\right\rangle$ to $\left|Q\overline{Q}\gamma\right\rangle$ with angular momentum quantum numbers which satisfy the selection rules $\Delta L = 0$ and $\Delta S = \pm 1$. Its probability is of order v^4

All the other states of the Fock space can be reached by a sequence of electric and magnetic transitions and their probability can be computed accordingly. Both electric and magnetic transitions change the color of a color singlet $Q\overline{Q}$ pair to a color octet.

The quarkonium state can thus be expanded in the Fock space:

$$\begin{aligned} \left|^{2S+1}L_J\right\rangle = \; & O(1)\left|^{2S+1}L_J^{[1]}\right\rangle + \\ & + O(v)\left|^{2S+1}(L \pm 1)_{J'}^{[8]}\right\rangle + \quad \text{(E1)} \\ & + O(v^2)\left|^{2(S\pm1)+1}L_{J'}^{[8]}\right\rangle + \quad \text{(M1)} \\ & + \ldots. \end{aligned} \tag{1.11}$$

1.3.8 Production factorization

In NRQCD the factorization between the short scale of the production and the long scale of the transition from the $Q\overline{Q}$ pair to the quarkonium is achieved quite naturally. The details of $Q\overline{Q}$ production, having an energy scale of order M, are parameterized in the coupling constants of the NRQCD operators, while the transition to quarkonium is described by the NRQCD interactions.

To describe the creation of a quarkonium state, local four-fields operators must be added to the Lagrangian (1.7):

$$\delta\mathcal{L}_{4\text{-fermions}} = \sum_i \frac{d_{ij}}{m_Q^2}(\psi^\dagger \mathcal{K}_i \chi)(\chi^\dagger \mathcal{K}_j \psi)$$

The factors $\mathcal{K}_i$, $\mathcal{K}_j$ are products of a spin and a color matrix and may also contain polynomials in the spatial gauge-covariant derivate $\vec{D}$. The operators in $\delta\mathcal{L}_{4\text{-fermions}}$ annihilate a $Q\overline{Q}$ pair in a color and angular momentum state specified by $\mathcal{K}_j$ and create a $Q\overline{Q}$ pair at the same space-time point in a state specified by$\mathcal{K}_i$. The probability of a $Q\overline{Q}$ pair with quantum numbers given by $\mathcal{K}_n$ to evolve into a certain quarkonium state with quantum numbers given by $\mathcal{K}_H$ is:

$$\left\langle \mathcal{O}^H[n] \right\rangle = \left\langle 0 \left| \chi^\dagger \mathcal{K}_H \psi \mathcal{P}_H \psi^\dagger \mathcal{K}_n \chi \right| 0 \right\rangle$$

where $\mathcal{P}_H$ projects onto states that in the asymptotic future contain the quarkonium state H plus soft partons S whose total energy is less than the ultraviolet cutoff Λ:

$$\mathcal{P}_H = \sum_S |H + S\rangle \langle H + S| .$$

The production cross section of a quarkonium H can thus be expressed as:

$$\sigma(H + X) = \sum_n \hat{\sigma}(Q\overline{Q}[n] + X) \left\langle \mathcal{O}^H[n] \right\rangle . \tag{1.12}$$

$\hat{\sigma}(Q\overline{Q}[n] + X)$ may be calculated perturbatively, while terms $\left\langle \mathcal{O}^H[n] \right\rangle$ are believed to be process independent and can be determined from phenomenology or calculated in lattice simulations. Moreover the long distance matrix elements can be related by spin symmetry (which is broken only with effects of order v^2), for example

$$\begin{aligned}
\left\langle \mathcal{O}^{\Upsilon(nS)}[^3P_J^{[8]}] \right\rangle &= (2J+1) \left\langle \mathcal{O}^{\Upsilon(nS)}[^3P_0^{[8]}] \right\rangle \\
\left\langle \mathcal{O}^{\chi_{bJ}}[^3S_1^{[8]}] \right\rangle &= (2J+1) \left\langle \mathcal{O}^{\chi_{b0}}[^3S_1^{[8]}] \right\rangle \\
\left\langle \mathcal{O}^{\chi_{bJ}}[^3P_J^{[1]}] \right\rangle &= (2J+1) \left\langle \mathcal{O}^{\chi_{b0}}[^3P_0^{[1]}] \right\rangle .
\end{aligned} \tag{1.13}$$

Besides the matrix elements of color singlet terms are related to the radial part of the wave function of potential models calculated in the origin and its derivatives ($|R(0)|$ and $|R'(0)|$):

$$\begin{aligned}
\left\langle \mathcal{O}^{\Upsilon}[^3S_1^{[1]}] \right\rangle &= \frac{N_c}{2\pi} |R(0)|^2 \left(1 + O(v^2)\right) \\
\left\langle \mathcal{O}^{\chi_{bJ}}[^3P_J^{[1]}] \right\rangle &= \frac{3N_c}{2\pi} (2J+1) |R'(0)|^2 \left(1 + O(v^2)\right)
\end{aligned} \tag{1.14}$$

where N_c is a color factor.

The expansion (1.12) is a double expansion:

- in α_s, as $\sigma(Q\overline{Q}[n] + X)$ is calculated perturbatively,
- in v, as from the velocity scaling rules of the fields of NRQCD and of the Fock states allow to deduce the scaling rule of $\left\langle \mathcal{O}^H[n] \right\rangle$.

In practical calculations some uncertainties arise: in hadroproduction the short distance cross sections must be convoluted with parton distribution functions. In addition the matrix elements are often poorly determined from phenomenology or lattice measurements and the large uncertainties on the heavy

quark masses ($\sim$ 8% for m_c and $\sim$ 2.4% for m_b) propagates to uncertainties on quarkonium rates which are proportional to a large power of the mass.

Despite NRQCD had many successes, for example it predicts accurately the J/ψ production yield observed at CDF, there still remain a number of discrepancies. For example according to this framework Υ and J/ψ should be produced almost fully transversely polarized ($J_z = \pm 1$) with respect to their own momentum direction (helicity frame) at high p_T as they are produced mainly by gluon fragmentation they should conserve the gluon transverse polarization. Such polarization however as not been observed.

1.4 THE χ_b STATES

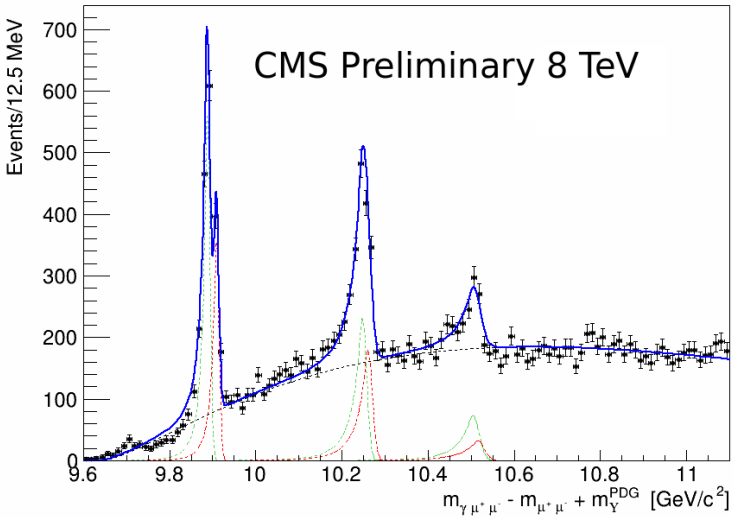

Figure 1.4.: Invariant mass obtained in CMS experiment with converted photons at $\sqrt{s} = 8$ TeV and $\mathcal{L} \approx 20$ fb^{-1}. The three radial excitations are clearly visible.

The observed P-waves of Bottomonium are the 1P, the 2P and, the recently discovered 3P. 1P and 2P states were first observed at Columbia University in 1983 and 1992 respectively, while the 3P state was first observed by ATLAS at LHC in December 2011 [30]. Tables 1.4 and 1.5 summarize the main properties of these particles.

Each radial excitation is a triplet with total angular momentum $J = 0, 1, 2$. The χ_{b0} states has a very low branching ratio to $\Upsilon\gamma$ so, radiative decays are mainly used to observe χ_{b1} and χ_{b2}. mainly observed.

Table 1.4.: χ_b states quantum numbers, $n = 1, 2, 3$.

Resonance	I^G	J^{PC}
$\Upsilon(1S)$	0^-	1^{--}
$\chi_{b0}(nP)$	0^+	0^{++}
$\chi_{b1}(nP)$	0^+	1^{++}
$\chi_{b2}(nP)$	0^+	2^{++}

Table 1.5.: Masses, branching ratios and Q-values of χ_b states from PDG. Masses are evaluated from the photon energy in a radiative decay so a double error is present: on the masses of the parent particle and on the photon energy.

Particle	Mass [MeV]	BR($\chi_b \to \Upsilon(1S) + \gamma$)	$\Delta m(\chi_b, \Upsilon)$ [MeV]
$\chi_{b0}(1P)$	$9859.44 \pm 0.42 \pm 0.31$	$(1.76 \pm 0.35)\%$	399.1
$\chi_{b1}(1P)$	$9892.78 \pm 0.26 \pm 0.31$	$(33.9 \pm 2.2)\%$	432.5
$\chi_{b2}(1P)$	$9912.21 \pm 0.26 \pm 0.31$	$(19.1 \pm 1.2)\%$	451.9
$\chi_{b0}(2P)$	$10232.5 \pm 0.4 \pm 0.5$	$(9 \pm 6) \cdot 10^{-3}\%$	772.5
$\chi_{b1}(2P)$	$10255.46 \pm 0.22 \pm 0.5$	$(9.2 \pm 0.8)\%$	795.2
$\chi_{b2}(2P)$	$10268.65 \pm 0.22 \pm 0.5$	$(7.0 \pm 0.7)\%$	808.4
$\chi_b(3P)$	$10539 \pm 4 \pm 8$	Unknown	899

Studying χ production can give important insights to understand QCD: production of ^3P_J states gives substantial feed-down contribution to the prompt production of $^3S_1$ states through electromagnetic decay; taking into account this effect may help to solve the disagreement between NRQCD and data concerning J/ψ and Υ polarization at hadronic colliders at high p_T. Moreover determining the cross section ratios between different χ states is an invaluable tool to understand the production mechanism as CEM, CSM and NRQCD give different predictions for these values and to constrain the relative magnitude of long distance matrix elements of NRQCD.

1.5 PRODUCTION CROSS SECTION RATIO OF χ_{b2} OVER χ_{b1}

Ratios of cross sections are important observables as many uncertainties cancel out, both theoretical (i. e. α_s, m_Q, $|R(0)|$ and

$|R'(0)|$, ...) and experimental (i.e. total luminosity, many contributions to efficiencies, ...). The ratio $\sigma(\chi_{b2})/\sigma(\chi_{b1})$ has not been previously measured while $\sigma(\chi_{c2})/\sigma(\chi_{c1})$ has been measured by CDF [14], CMS [18] and LHCb [19]. The results of these three measurements are summarized in figure 1.6

1.5.1 Theoretical predictions

CEM and CSM

The color evaporation model predicts the ratio to be always 5/3 based on spin counting in all orders of α_s [28]. The prediction for the color singlet model can be deduced by the one of NRQCD neglecting color-octet matrix elements. If color octet terms will not be needed to explain experimental results, then CSM will be corroborated.

NRQCD LO

With the short distance differential cross sections evaluated at leading order (LO) in α_s, NRQCD predicts the χ_c production cross sections to scale as $1/{p_T}^6$ in the color singlet channels and scale as $1/{p_T}^4$ in the color octet channel. Thus the color octet contribution would dominate at large p_T predicting from (1.13) the ratio $\sigma_{\chi_{c2}}/\sigma_{\chi_{c1}}$ to be 5/3, as one would obtain from spin counting. All three measurements disagree with these predictions.

NRQCD NLO(α_s) LO(v)

The authors of [28] study how the p_T dependence changes taking into account also next-to-leading order (NLO) in α_s. Considering NLO in α_s and LO in v only two matrix elements are involved: the color singlet term $\left\langle O^{\chi_J}[{}^3P_J^{[1]}]\right\rangle$ and the color octet $\left\langle O^{\chi_J}[{}^3S_1^{[8]}]\right\rangle$. They found out that the color singlet channel scales like $1/{p_T}^4$ for high p_T in contrast to $1/{p_T}^6$ at LO. In the high p_T region this term seems negligible at LO, but at NLO it is comparable to the color octet channel. They found also that the ${}^3P_1^{[1]}$ channel decreases slower than the ${}^3P_2^{[1]}$ and this can justify why the production of χ_{b1} exceeds the one of χ_{b2} at high p_T which CEM does not predict.

To evaluate the importance of including also the color octet term, and use NRQCD instead of simple CSM, they define

$$r = \frac{\left\langle O^{\chi_0}[{}^3S_1^{[8]}]\right\rangle}{\left\langle O^{\chi_0}[{}^3P_J^{[1]}]\right\rangle / m_c^2}\Big|_{\overline{MS},\,\mu_\Lambda = m_c}$$

so that

$$\sigma(\chi_{c2})/\sigma(\chi_{c1}) = \frac{5}{3}\frac{r\,d\hat{\sigma}({}^3S_1^{[8]}) + d\hat{\sigma}({}^3P_2^{[1]})}{r\,d\hat{\sigma}({}^3S_1^{[8]}) + d\hat{\sigma}({}^3P_1^{[1]})}.$$

By fitting data from [14] they obtained $r \approx 0.27 \pm 0.06$. The color octet contribution seems thus not negligible.

NRQCD LO(α_s) NLO(v)

Authors of [27] instead search a solution to the disagreement between data and NRQCD at LO studying NLO in v but keeping short distance cross sections at LO in α_s. The Fock state expansion (1.11) of the χ_c then reads

$$\begin{aligned}|\chi_{cJ}\rangle = &\left\langle O^{\chi_{cJ}}[^3P_J^{[1]}]\right\rangle \left|^3P_J^{[1]}\right\rangle + \left\langle O^{\chi_{cJ}}[^3S_1^{[8]}]\right\rangle \left|^3S_1^{[8]}\right\rangle \\ &+ \left\langle O^{\chi_{cJ}}[^1P_1^{[8]}]\right\rangle \left|^1P_1^{[8]}\right\rangle + \sum_{J'} \left\langle O^{\chi_{cJ}}[^3P_{J'}^{[8]}]\right\rangle \left|^3P_{J'}^{[8]}\right\rangle \\ &+ \dots .\end{aligned} \tag{1.15}$$

where the first two terms are $O(v)$ and the next two are $O(v^2)$. Using spin symmetry (1.13) and the relation with the radial part of the wave function (1.14) they reduce the number of free parameters to be determined from data. Then they performed a fit on CDF χ_c production data [13] and on the measurements of $\sigma(\chi_{c2})/\sigma(\chi_{c1})$ [14, 18, 19] to extract the missing long distance matrix elements. The result of the fit along with the p_T dependence of the various short distance cross sections are reported in figure 1.5.

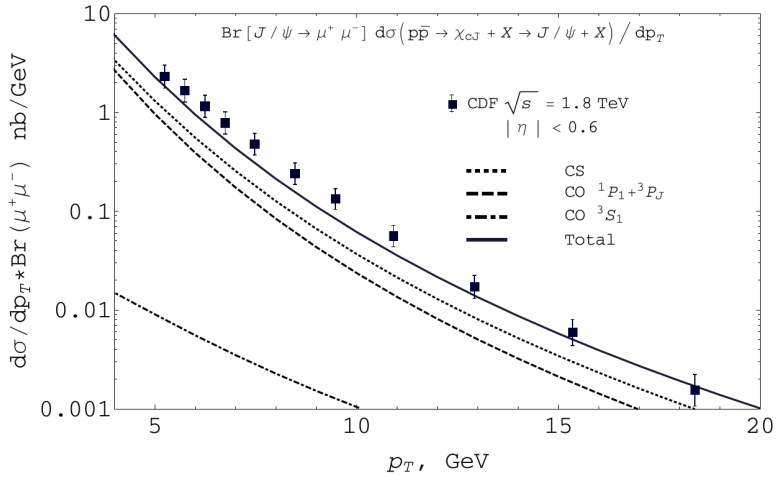

Figure 1.5.: Contributions to the χ_c production from different states. Dotted line is the color singlet contribution. Dashed line is a contribution from the octet $\left|^3P_J^{[8]}\right\rangle$ and $\left|^1P_1^{[8]}\right\rangle$ states. Dot-dashed line is color-octet $\left|^3S_1^{[8]}\right\rangle$ state contribution. Solid line is a sum over all contributions. Experimental points are taken from CDF results [13].

Having constrained the χ_c matrix elements they argue that the corresponding matrix elements for χ_b can be found assuming:

1. the relative contribution from different Fock states similar from bottomonium to charmonium mesons and not depending on the radial excitation number:

$$\frac{\left\langle O^{\chi_c}[^3P_J^{[8]}]\right\rangle}{\left\langle O^{\chi_c}[^3P_J^{[1]}]\right\rangle} = \frac{\left\langle O^{\chi_b(nP)}[^3P_J^{[8]}]\right\rangle}{\left\langle O^{\chi_b(nP)}[^3P_J^{[1]}]\right\rangle}$$

2. from the dimensional analysis $\left\langle O^H[^3P_J^{[1]}]\right\rangle \sim M^2 \cdot \left\langle O^H[^3S_1^{[8]}]\right\rangle$ so that

$$\frac{\left\langle O^{\chi_c}[^3S_1^{[8]}]\right\rangle}{\left\langle O^{\chi_c}[^3P_J^{[1]}]\right\rangle} = \frac{M^2_{\chi_b}}{M^2_{\chi_c}} \frac{\left\langle O^{\chi_b}[^3S_1^{[8]}]\right\rangle}{\left\langle O^{\chi_b}[^3P_J^{[1]}]\right\rangle}.$$

The picture of bottomonium production is then complete as the short distance cross sections are the same of charmonium. In figure 1.6 the three measurements of $\sigma(\chi_{c2})/\sigma(\chi_{c1})$, the fit and the prediction of $\sigma(\chi_{b2})/\sigma(\chi_{b1})$ are summarized.

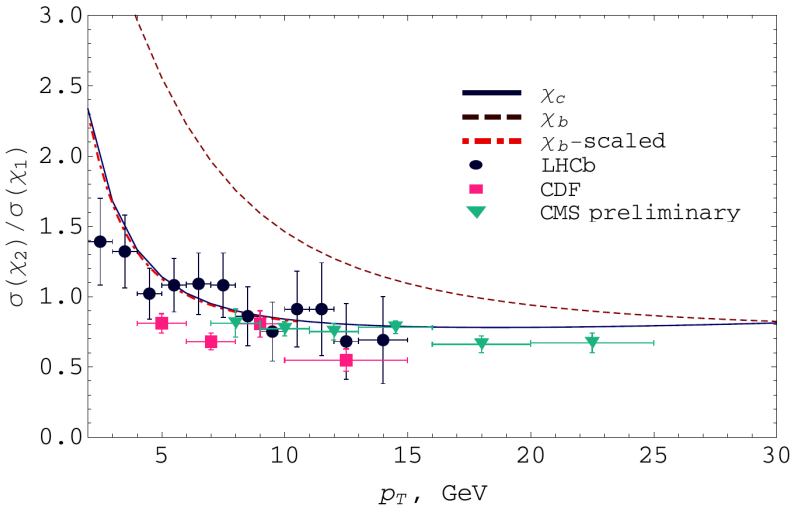

Figure 1.6.: Transverse momentum distributions of the $\sigma(\chi_2)/\sigma(\chi_1)$. Solid and dashed lines stand for charmonium and bottomonium mesons. The dot-dashed line corresponds to the rescaled bottomonium ratio: $\sigma_{b2}/\sigma_{b1}(M_{\chi_c}/M_{\chi_b}p_T)$. As it is seen, it almost matches the charmonium curve. The experimental results for charmonium from LHCb [19] are shown with dots, from CDF [14] with rectangles, and from CMS [18] with triangles.

2 THE CMS EXPERIMENT AT LHC

The present chapter gives a short description of the Large Hadron Collider (LHC) and focuses on the Compact Muon Solenoid (CMS) experiment.

2.1 THE LARGE HADRON COLLIDER

The Large Hadron Collider (LHC) [5, 7, 8] is the world's largest and highest energy particle accelerator ever built. Proposed and realized by the European Organization for Nuclear Research (CERN), it was design to collide protons, as well as lead ions, at an unprecedented energy and rate, in order to address some of the most fundamental questions of physics.

2.1.1 LHC design and performances

The LHC lies in the already existent 26.7 km long LEP tunnel, situated at a depth of about 100 m underground at the boundary between Switzerland and France. The main design characteristics are listed in table 2.1

Table 2.1.: LHC design parameters for p-p and Pb-Pb collisions.

Parameter	p - p	Pb - Pb
Circumference [km]	26.659	
Beam radius at interaction point	15	
Dipole peak field [T]	8.3	
Design center of mass energy [TeV]	14	1148
Design Luminosity [$cm^{-2}s^{-1}$]	10^{34}	$2 \cdot 10^{27}$
Luminosity lifetime [h]	10	4.2
Number of particles per bunch	$1.1 \cdot 10^{11}$	$\sim 8 \cdot 10^{7}$
Number of bunches	2808	608
Bunch length [mm]	53	75
Time between collisions [ns]	24.95	$124.75 \cdot 10^{3}$
Bunch crossing rate [MHz]	40.08	0.008

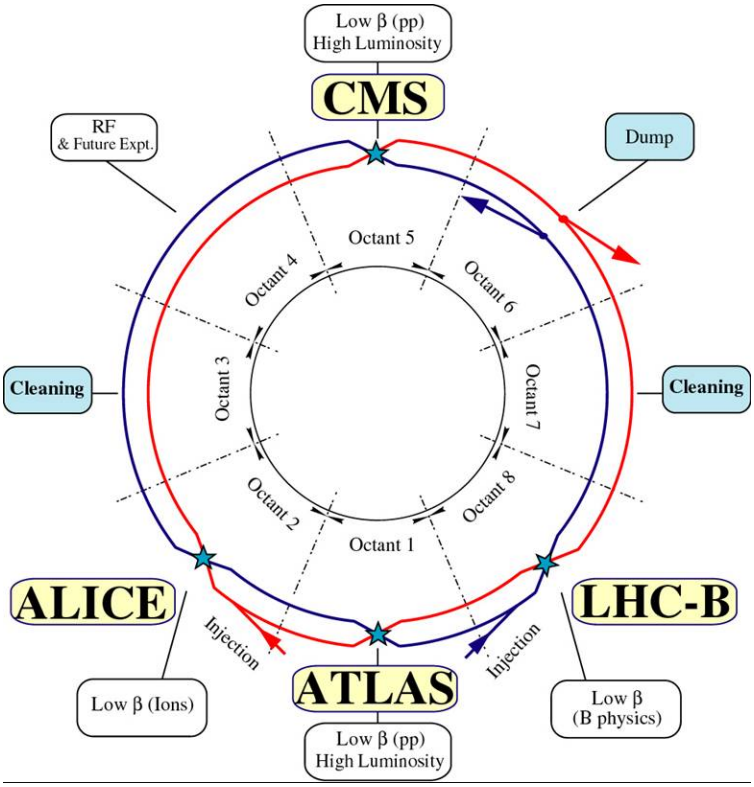

Figure 2.1.: A schematic picture of the LHC layout

Since collisions occur between particles of the same charge, the tunnel contains two adjacent and parallel beam pipes, where proton (or ion) beams travel in opposite directions and intersect in four points, where the main experimental halls are built and detectors are placed (see figure 2.1).

Magnets

Some 1232 dipole magnets keep the beams on their circular path, while additional 392 quadrupole magnets are used to keep the beams focused, in order to maximize the chances of interaction in the four intersection points, where the two beams cross. In total, over 1600 superconducting magnets are installed. Approximately 96 tonnes of liquid helium is needed to keep the superconducting magnets at their operational temperature of 1.9 K. The field in the magnets increase from 0.53 T to 8.3 T while the protons are accelerated from 450 GeV to 7 TeV.

Accelerating steps

Before being injected into the main accelerator, the protons are prepared by a series of systems that successively increase their energy (see figure 2.2). The first system is the linear particle accelerator (LINAC 2) generating 50 MeV protons, which feeds the Proton Synchrotron Booster (PSB). There the protons are accelerated to 1.4 GeV and injected into the Proton Synchrotron (PS),

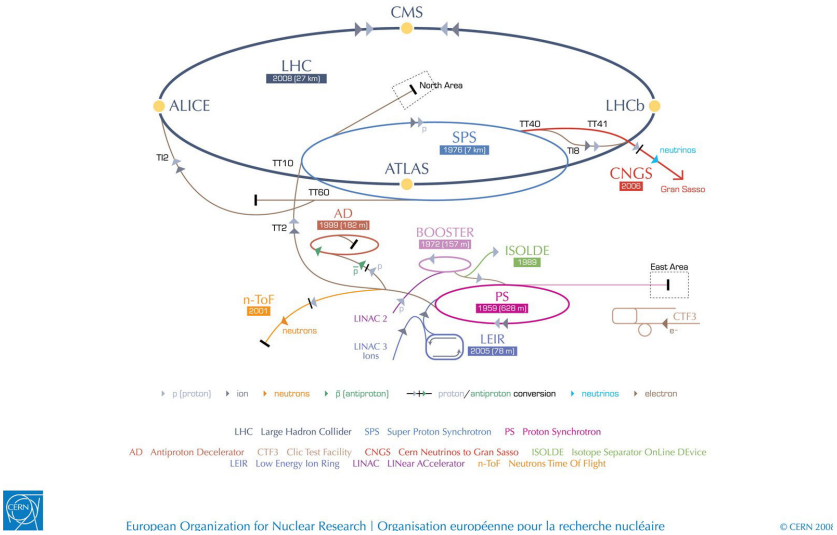

Figure 2.2.: CERN's accelerator complex

where they are accelerated to 26 GeV. Finally the Super Proton Synchrotron (SPS) is used to further increase their energy up to 450 GeV before they are at last injected into the main ring. Here the proton bunches are accumulated, accelerated (over a period of 20 minutes) to their peak energy, and finally circulated while collisions occur at the four intersection points (IP).

Luminosity

Two of the main experiments, ATLAS and CMS, are designed for a high luminosity regime, in order to catch the rare events of their physics programs. For this reason the beam intensity, together with the beam energy, is a crucial parameter for the LHC. Assuming a Gaussian beam shape, the luminosity at LHC can be written in terms of machine parameters as:

$$\mathcal{L} = \frac{N_b \cdot n_b \cdot f_{rev} \cdot \gamma}{4\pi \cdot \varepsilon_n \cdot \beta^*} F$$

where:

N_b is the number of particles per bunch,

n_b is the number of bunches per beam,

f_{rev} is the revolution frequency,

γ is the Lorentz factor,

ε_n is the normalized transverse beam emittance,

β^* is the optical Beta function at the collision points,

F is the geometric luminosity reduction factor due to crossing angle at the intersection points.

2.1.2 The LHC experiments

The Large Hadron Collider hosts six different experiments; each experiment has a different composition and geometry of the subdetectors so that it is more specialized in a particular area of the research in particle physics.

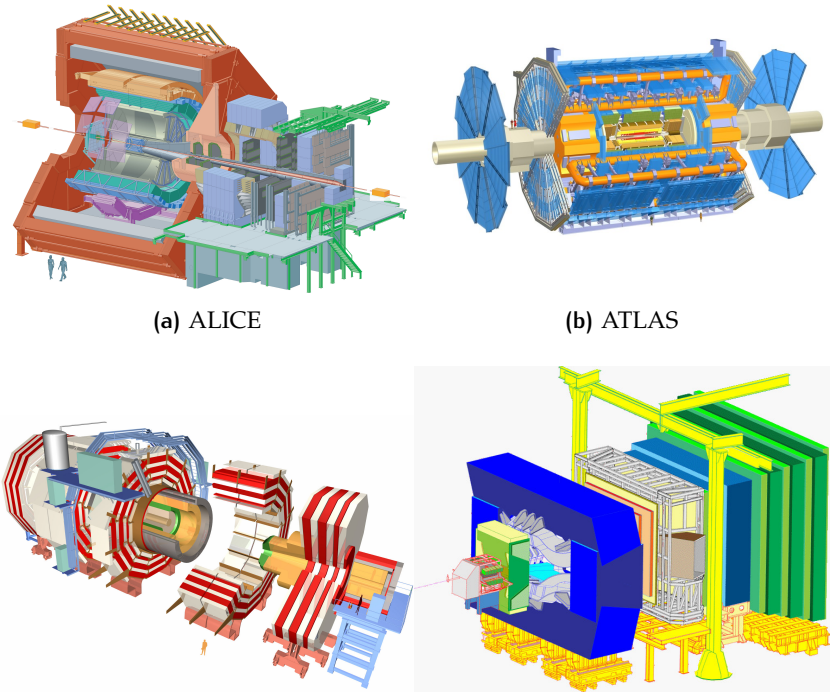

(a) ALICE **(b)** ATLAS

(c) CMS **(d)** LHCb

Figure 2.3.: LHC's four main experiments

ALICE

ALICE (A Large Ion Collider Experiment) is a detector optimized for PbPb collisions, in particular for the study of the properties of matter at high temperature and high energy density generated by such collisions (Quark Gluon Plasma).

ATLAS & CMS

ATLAS (A Toroidal Lhc ApparatuS) and CMS (Compact Muon Solenoid) are two general-purpose, high-luminosity detectors; they are built with a cylindrical geometry around the beamline. Even if theoretically "general-purpose" detectors these two have been designed with the discovery of new physics in the TeV scale, thus their subdetectors are optimized for the reconstruction of high energy objects with great efficiency and accuracy. These two detectors will be able to measure masses of new particles produced by collisions up to 3-4 TeV. While similar in their purposes, the design of the two detectors differs significantly, since different solutions were chosen for the configuration of the mag-

netic field. ATLAS uses a toroidal field produced by three sets of air-core toroids complemented by a small solenoid in the inner region, while CMS uses a solenoidal field generated by the world's largest superconducting solenoid.

LHCb

LHCb is specialized in studies regarding the physics of heavy quarks and heavy mesons with a particular attention to the b quark and its mesons.

TOTEM & LHCf

TOTEM (TOTal Elastic and diffractive cross section Measurement) and LHCf ("f" stands for forward) are forward detectors of CMS and ATLAS repectively, they are placed $\sim$ 100 m from the interaction points of the main experiments to study diffractive physics happening in the very forward region of the collision. These detectors were to be put far from the interaction point so that the products of such very forward (i.e. small angle with respect to the beamline) inelastic or elastic collisions may exit the beampipe.

2.2 CMS

CMS [9] is one of the four main experiments at LHC. Its primary goals are the study of the electroweak symmetry breaking mechanism linked to the Higgs mechanism, the search for physics Beyond the Standard Model (BSM) and the precision measurements of already known physics processes. In order to fulfill these goals, excellent lepton reconstruction and particle identification are required. A particular magnetic field configuration is necessary to provide a large bending power and to have thus good resolution in measuring charge particles of high momentum.

2.2.1 General overview coordinate system and kinematic variables

Overview

The central feature of the Compact Muon Solenoid (CMS) apparatus is a superconducting solenoid of 6 m internal diameter, providing a field of 3.8 T. Within the field volume are a silicon pixel and strip tracker, a crystal electromagnetic calorimeter (ECAL) and a brass/scintillator hadron calorimeter (HCAL). Muons are measured in gas-ionization detectors embedded in the steel return yoke. Extensive forward calorimetry complements the coverage provided by the barrel and endcap detectors.

The overall structure of CMS consists of several cylindrical layers coaxial to the beam axis (the barrel layers), closed at both

ends by detector disks orthogonal to the beam direction (the endcaps), to ensure optimal hermeticity. The CMS apparatus has an overall length of 22 m, a diameter of 15 m, and weighs 14 000 tonnes. A schematic view of the CMS detector is shown in Figure 2.4.

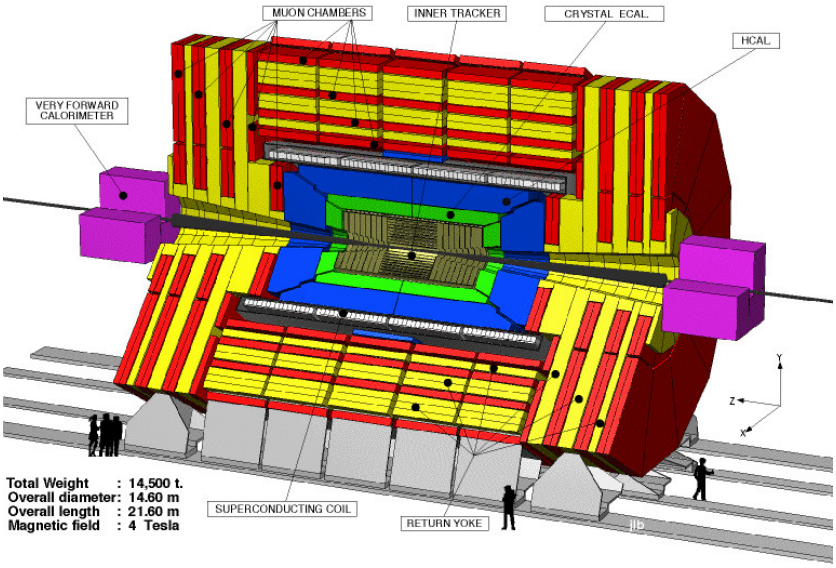

Figure 2.4.: A tree dimensional view of the CMS detector

Coordinate system

CMS uses a right-handed coordinate system, with the origin at the nominal interaction point, the x axis pointing to the center of the LHC, the y axis pointing up (perpendicular to the LHC plane), and the z axis along the anticlockwise-beam direction. The polar angle ϑ is measured from the positive z axis and the azimuthal angle ϕ is measured in the x-y plane (transverse plain) from the positive x axis.

Kinematic variables

For a particle carrying quadrimomentum (E, p_x, p_y, p_z), the momentum vector $\vec{p}$ can be divided in two components: the longitudinal momentum p_z and the transverse momentum $p_T = \sqrt{p_x^2 + p_y^2}$. This decomposition is sensible in hadron colliders where the energy of the colliding partons is unknown. A good fraction of the proton energy is carried by the proton remnants which are scattered at small angles and, remaining in the beam pipe, are not detected. The speed of the interaction point is thus unknown, for this reason it is useful to use variables with good transformation properties under Lorentz boosts as the p_T, which is invariable, and the *rapidity* defined by

$$y = \frac{1}{2} \ln \frac{E + p_z}{E - p_z}$$

which transforms with a simple additive law. For ultra-relativistic particles ($E \sim |\vec{p}|$) the rapidity can be approximated by the *pseudorapidity*

$$\eta = -\ln\left(\tan\frac{\vartheta}{2}\right)$$

which is often referred to at the place of ϑ.

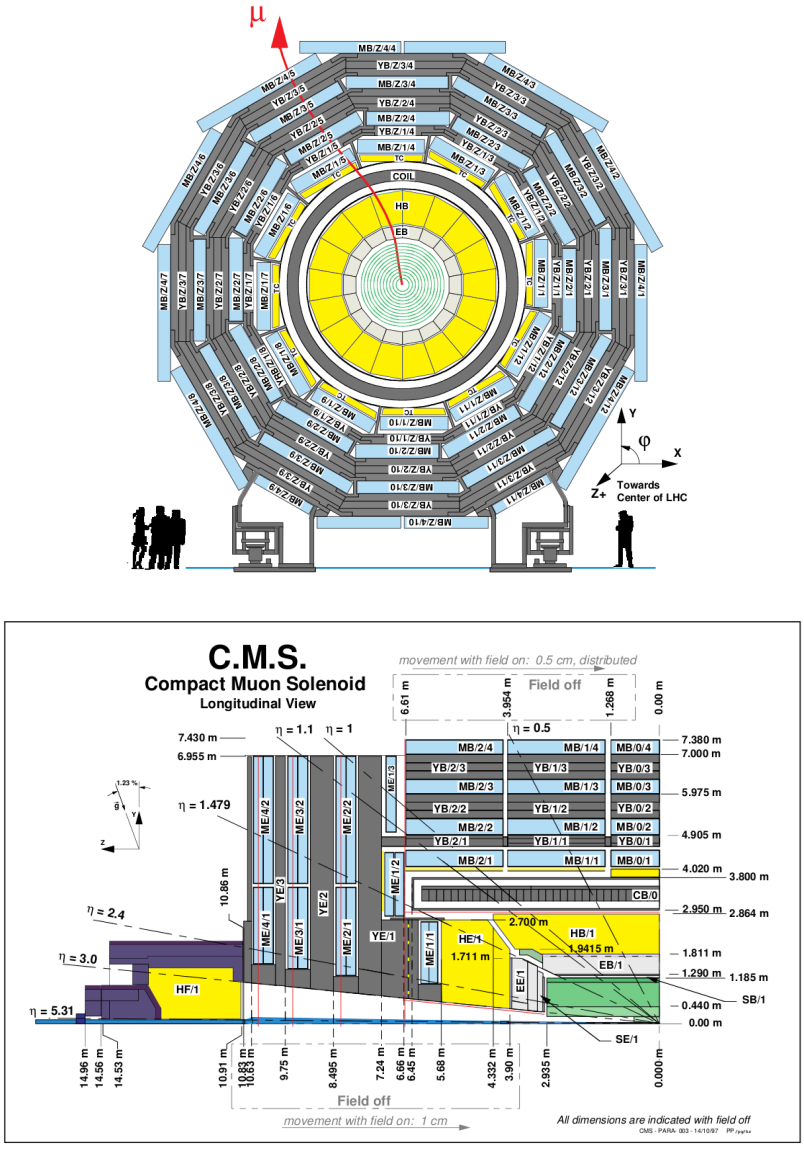

Figure 2.5.: Section and side view of the CMS detector

2.2.2 Sub-systems

Tracking system

The Tracker is the CMS innermost sub-detector and the closest to the interaction point. Its purpose is to reconstruct high-p_T charged tracks with high efficiency and momentum resolution, to measure their impact parameter and to reconstruct primary and secondary vertices. It extends in the region of $|\eta| < 2.5$, $r < 120$ cm, $|z| < 270$ cm and it is completely based on semiconductor detectors made of silicon, that cover a total surface of 210 m^2.

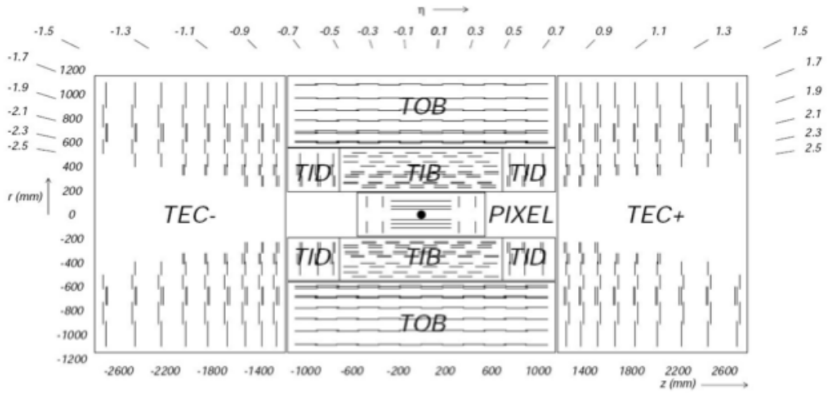

Figure 2.6.: Schematic representation of the tracking system

Pixel Detector

The pixel detector [17] provides high-resolution three-dimensional measurement, that is used for charged track reconstruction. It consists of three barrel layers at $r = 4.4$ cm, 7.3 cm, 10.2 cm and 53 cm long in z and 2 endcap disks at $|z| = 34.5$ cm and 46.5 cm, with 6 cm $< r <$ 15 cm. In order to get a good vertex resolution high granularity is required: about 66 million pixels 100 μm × 150 μm wide allow a resolution of about 10 μm in the transverse plane and 20 μm along z. This excellent resolution allows the measurement of track impact parameters, the identification of b-jets and τ-jets and the reconstruction of vertices in three dimensions.

Microstrip Detector

The microstrip detector is divided in two main regions. The inner part consists of four barrel layers and nine forward disks. The full tracker consists of about 15 000 microstrip detectors, covering a radial region between 20 and 120 cmand the pseudorapidity region $|\eta| < 2.5$. It provides a spatial resolution of about 50 μm in the transverse plane and 500 μm along z.

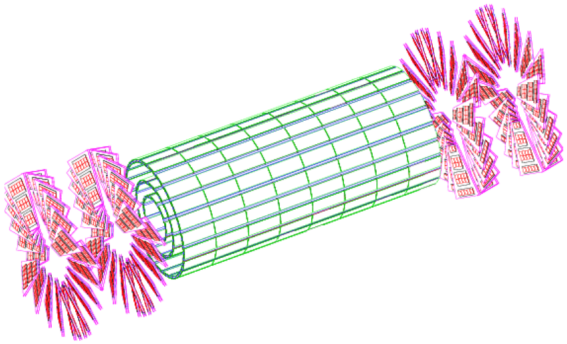

Figure 2.7.: Schematic illustration of the pixel detector

Electromagnetic Calorimeter

The electromagnetic calorimeter [16] consists of 75 848 lead tungstate ($PbWO_4$) crystals which provide coverage in pseudo-rapidity $|\eta| < 1.479$ in a barrel region (EB) and $1.479 < |\eta| < 3.0$ in two endcap regions (EE). A preshower detector consisting of two planes of silicon sensors interleaved with a total of $3X_0$ of lead is located in front of the endcap.

Its goal is the identification and measurement of the energy of electrons and photons. It has an energy resolution of better than 0.5% for unconverted photons with transverse energies above 100 GeV and 3% or better for electrons. Lead tungstate is a transparent material characterized by a high density (8.28 g/cm^3), a short radiation length (X_0 = 0.89 cm) and a small Molière radius (2.2 cm). These features allow a very compact shape and a fine granularity, necessary because of the high particle density produced at the LHC. Moreover, these crystals have a trapezoidal shape and they are characterized by a very short scintillation decay time, which permits to collect about 80% of the light within 25 ns, so that they can be used at the crossing rate of 40 MHz.

Hadron Calorimeter

The Hadron Calorimeter (HCAL) surrounds ECAL and its design is strongly influenced by the choice of the magnet parameters and by the fact that most of it is placed inside the magnet coil. This detector plays an essential role in the identification and measurement of hadrons by estimating the energy and the direction of jets. It is also used for neutrino detection by measuring the missing transverse energy of the event. For this reason, one of the main design requirements is a high hermeticity. In particular, the HCAL angular coverage must include the very forward region, since the identification of forward jets is very important

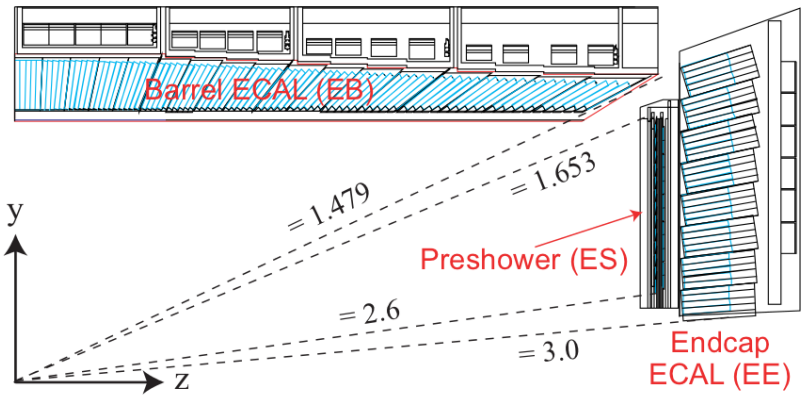

Figure 2.8.: Schematic view of the electromagnetic calorimeter

for the rejection of many backgrounds and the evidence of BSM signatures.

The HCAL is a sampling calorimeter, that meaning it finds particles position, energy and arrival time using alternating layers of "absorber" and "scintillator" materials. In particular, brass was chosen as absorber material, thanks to its non magnetic behavior and its quite short interaction length ($\lambda_I \sim 151$ mm). To maximize the amount of absorber before the magnet, the space devoted to the active medium is minimized. The active part is made of scintillator tiles coupled with wavelength shifting fibers and clear fibers carrying the light to the readout system.

The Hadronic Calorimeter can be divided in four parts, that permit a good segmentation, a moderate energy resolution and a full angular coverage. The barrel hadronic calorimeter (HB) surrounds the electromagnetic calorimeter and covers the central pseudorapidity region up to $|\eta| = 1.3$. The endcap regions are covered up to $|\eta| = 3$ by the two endcap hadron calorimeters (HE). The HB and HE are located inside the solenoid magnet. To satisfy the hermeticity requirements, forward calorimeters are placed outside the magnet yoke, 11 mfar from the interaction point, extending the pseudorapidity coverage up to $|\eta| = 5$. Finally, an array of scintillators located outside the magnet, which is referred to as the outer hadronic calorimeter (HO), is used to improve the central shower containment.

The superconducting magnet

The CMS magnet [3] is a 13 m long superconducting solenoid. It is able to generate a uniform magnetic field of 4 T in the inner region, storing about 2.5 GJ of energy. It operates at a temperature of 4 K, ensured by a sophisticated helium cooling system.

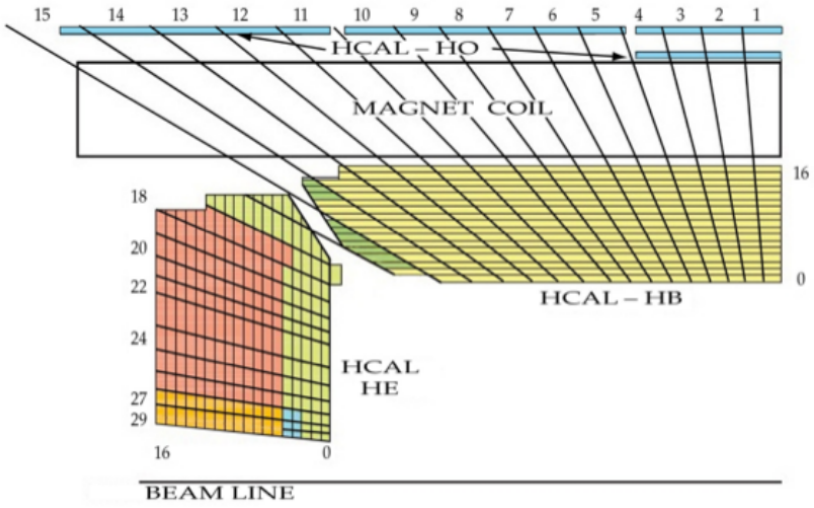

Figure 2.9.: Schematic view of the hadronic calorimeter

At such temperatures, the flat NiTb cable becomes superconducting, allowing a 20 kA current to flow without appreciable loss.

The whole magnet is contained in a enormous vacuum cylinder, which isolates it from the external environment. Outside, an iron structure composed by five barrel layers and three disks for each endcap constitutes the iron yoke, needed to guide the return magnetic field, which would get lost otherwise, causing interferences. The CMS magnet provides a huge bending power, allowing a precise measurement of the transverse momentum of charged particles inside the solenoid, operated by the inner tracking system. A further and independent p_T measurement outside the solenoid is possible thanks to the iron yoke, which surrounds the muon chambers.

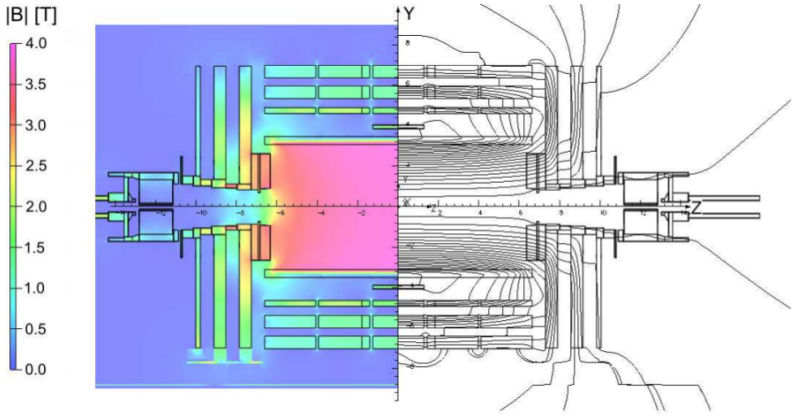

Figure 2.10.: The CMS magnet and the generated magnetic field

Muon system

Because muons can penetrate several meters of iron without being stopped, they are detected by muon chambers, placed in the outermost part of the experiment. The muon detection system [15] is therefore set outside the magnetic coil and it has multiple tasks: triggering on muons, identifying them and assisting the tracker in measuring their momentum. The minimum value of the muon transverse momentum required to reach the system is about five GeV. Matching muons to tracks measured in the silicon tracker results in a transverse momentum resolution between 1 and 5%, for p_T values up to 1 TeV

Muons are measured in the pseudorapidity range $|\eta| < 2.4$, with detection planes made using three technologies: *drift tubes* (DT, $|\eta| < 1.2$), *cathode strip chambers* (CSC, $0.9 < |\eta| < 2.4$) and resistive plate chambers (RPC, $|\eta| > 1.2$). The detector can thus be divided in three regions, referred to as *barrel* ($|\eta| < 0.9$), *overlap* ($0.9 < |\eta| < 1.2$) and *endcap* ($|\eta| > 1.2$). The reason for these different technologies lies in the different particle rates and occupancies, both higher in the endcaps, and in the intensity of the stray magnetic field, which is lower in the barrel.

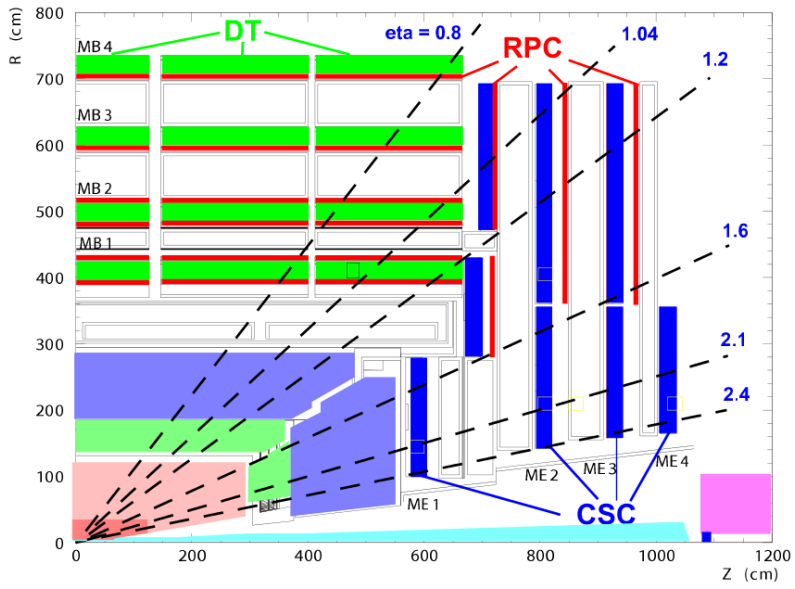

Figure 2.11.: Schematic view of the Muon system

Drift tubes

In the barrel the track density and the residual magnetic field are low, here are installed four layers of drift tubes. The chamber segmentation follows that of the iron yoke, consisting of five wheels along the z axis, each one divided into twelve azimuthal

sectors. Each chamber has a resolution of about 100 μm in the transverse plane and 1 mrad in ϕ.

Cathode strip chambers

In the endcaps where there is a hight particle rate and a large residual magnetic field between the plates of the yoke, are placed four disks (stations) of cathode strip chambers. The rings are formed by 18 or 36 trapezoidal chambers, which are stacked with a small overlap in ϕ. These chambers have a spatial resolution of about 200 m (100 m for the chambers belonging to the first station) and 10 mrad in $r - \phi$.

Resistive plate chambers

Redundancy is obtained with a system of resistive plate chambers, that are installed in both the barrel and the endcaps. They have limited spatial resolution, but fast response and excellent time resolution of few ns, providing unambiguous bunch crossing identification. these detectors operate in avalanche mode, thus allowing them to sustain higher rates. This mode is obtained with a lower electric field, thus the gas multiplication is reduced and an improved electronic amplification is required. In the barrel the RPC chambers follow the segmentation of DT chambers. A total of six layers of RPCs are present. In the endcaps the chambers are trapezoidal distributed on four disks. They are also used to complement DTs and CSCs in the measurement of p_T.

The robustness of the spectrometer is also guaranteed by the different sensitivity of DT, RPC and CSC to the background: the request of correlation between consecutive layers is thus particularly effective against background hits affecting only a single layer. Thanks to the fast response they provide, all the muon detectors are also used within the first level of the trigger system.

2.2.3 Trigger

The huge amount of data produced due to the high interaction rate produced at LHC cannot be sustained by any storage system presently available. Given the typical size of a raw event (1 MB), only a rate of $\sim$ 100 Hz can be stored for offline analysis, when the collisions rate is in fact 40 MHz. A huge reduction factor is thus necessary.

The event rate is mainly composed of protons interactions with particles of low transverse momentum. A good triggering system should have a large rejection of the less interesting events and maintain at the same time a high efficiency on the (potential) interesting ones. This characteristic is achieved at CMS in two steps: a Level 1 Trigger (L1) and a High Level Trigger (HLT). The rate reduction capability is designed to be a factor of 107 for the combined L1 and HLT.

The Level 1 Trigger

The Level 1 Trigger consists of custom-designed, largely programmable electronics: it reduces the rate of selected events down to 100 kHz for the high luminosity runs. The full data are stored in pipelines of processing elements, while waiting for the trigger decision. The maximum latency allowed is 3.2 μs: if the L1 accepts the event, the data are moved to be processed by the High Level Trigger. The high bunch crossing rate does not permit the full readout of the detector, mainly because of the slowness of the tracker algorithms: only the calorimetric and muons information are employed. The Calorimeter Trigger identifies the best four candidates of each of the following classes: electrons and photons, central jets, forward jets and so on identified from the shape of the deposited energy. The information of these objects is passed to the Global Trigger, together with the measured missing E_T . The Muon trigger is performed separately for each muon detector. The information is then merged and the best four muon candidates are transferred to the Global Trigger. The Global Trigger takes the decision to reject an event or to accept the event for further evaluation by the HLT. The decision is based on algorithm calculations and on the readiness of the sub-detectors and the DAQ. The L1 Trigger electronics is housed partly on the detectors, partly in the underground control room located at a distance of approximately 20m from the CMS detector site.

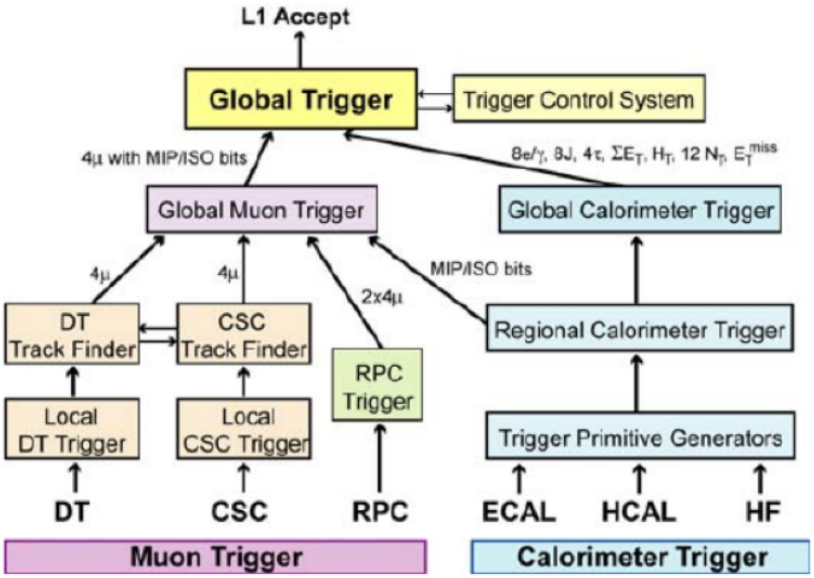

Figure 2.12.: Scheme of the L1 trigger

The High Level Trigger (HLT)

HLT is a software system (implemented in a filter farm of about one thousand commercial processors) which reduces the output rate down to around 100 Hz. The idea of the HLT trigger software is the regional reconstruction on demand: only objects in the useful regions are reconstructed and uninteresting events are rejected as soon as possible. The HLT has access to the high-resolution data in pipelined memories in the front-end electronics as well as the information from the silicon tracker: it can therefore perform complex calculations. The L1 and HLT schema lead to the development of three "virtual trigger" levels: at the first level only the full information of the muon system and of the calorimeters is used, in the second level the information of the tracker pixels is added and in the third and final level the full event information is available.

The Data Acquisition (DAQ)

The CMS Data Acquisition (DAQ) has the task to transport the data from about 650 data sources at the detector side, to the filter units for processing of complete events. Each data source provides event fragments of about 2 kB. The central DAQ runs online software on about 3000 PC used for buffering and processing of event data. The detector is read out through a builder network with a bandwidth of 100 GB/s by the so called Front-End Drivers (FED). The FEDs are located in the underground counting room $\sim$ 70 m from the detector. Complete events are fed to the event filter systems at a rate of maximal 100 kHz. The large rate to the filter systems stems from the design choice of CMS to build the full event already after the first level trigger instead of building partial events as in traditional multi level trigger systems. This requires the read-out, assembly and forwarding of the full event data at the nominal level one trigger rate. The total rate of data produced by the online trigger system is $\sim$ 230 MB/s. These data need to be stored for further processing and analysis.

2.2.4 Software framework

CMS computing and storage requirements is, with present technology, impossible to fulfil in only one place, for both technical and funding reasons. Therefore, the CMS computing environment has been constructed as a distributed system of computing services and resources that interact and cooperate with each other, as *Grid* services. The set of services and computing

resources are used for storage, connectivity resources, data processing, data archiving, Monte Carlo event generation and all kinds of computing-related activities.

Grid computing aims to provide reliable and secure access to widely scattered resources for authorized users located virtually anywhere in the world. When a user submits a job, the Grid software controls where the job gets sent for processing.

A 3-level Tier structure of computing resources has been organized to handle the vast storage and computational requirements of the CMS experiment. A CMS physicist may use Grid tools to submit a CMS analysis job to a "Workload Management System" (WMS), and does not need to worry about the details such as location of data and available computing power, which are handled transparently.

The CMS Grid system is part of the larger Worldwide LHC Computing Grid Project (WLCG). The mission of the WLHC Computing Project (WLCG) is to build and maintain a data storage and analysis infrastructure for the entire high energy physics community that will use the LHC. The WLCG project aims to collaborate and interoperate with other major Grid development projects and production environments around the world. As such, WLCG has developed relationships with regional computing centres as T1 centres. These centres exist in a number of different countries in Europe, North America and Asia.

As stated just above, the computing centres available to CMS through the Grid system around the world are distributed and configured in a "tier" architecture. Each of the three tier levels provides different resources and services:

- Tier-0, the first tier in the CMS model, for which there is only one site, CERN. Among its tasks there are: accept, archive and distribute RAW data collected from the CMS Online Data Acquisition and Trigger System (TriDAS), perform Prompt calibration in order to get the calibration constants needed to run the reconstruction, perform prompt first pass reconstruction which writes the RECO and Analysis Object Data (AOD) extraction, transfer Prompt reconstructed RECO and AOD datasets to Tier-1.

- Tier-1: there is a set of seven Tier-1 (T1) sites, which are large centers in CMS collaborating countries (large national labs o research institutes, e.g. INFN, and FNAL) Among its tasks there are: archive and redistribute to Tier-2 RAW, RECO, AOD and MC samples,

- Tier-2: this is a more numerous set of smaller centres, but with substantial CPU resources, providing capacity for user

analysis, calibration studies, and Monte Carlo production. Tier-2 provide limited disk space, and no tape archiving. T2 centers rely upon T1s for access to large datasets and for secure storage of the new data (i.e. Montecarlo simulations) produced at the T2.

CMS Data is arranged into a hierarchy of data tiers. Each physics event is written into each data tier, where the tiers each contain different levels of information about the event. The three main data tiers used in CMS are:

- RAW: full event information from the Tier-0 (i.e. from CERN), containing 'raw' detector information (detector element hits, detailed trigger information, various electronic info). Not used directly for analysis.
- RECO ("RECOnstructed data"): the output from first-pass processing by the Tier-0. This layer contains reconstructed physics objects and part of RAW info, thus it's still very detailed and may slow down analysis when CMS has collected a substantial data sample.

  The event reconstruction step from RAW to RECO is structured in several hierarchical steps:

  1. Detector-specific processing: Starting from detector data unpacking and decoding, detector calibration constants are applied and cluster or hit objects are reconstructed.
  2. Tracking: Hits in the silicon and muon detectors are used to reconstruct global tracks. Pattern recognition in the tracker is the most CPU-intensive task.
  3. Vertexing: Reconstructs primary and secondary vertex candidates.
  4. Particle identification: Produces the objects most associated with physics analyses. Using a wide variety of sophisticated algorithms, standard physics object candidates are created (electrons, photons, muons, missing transverse energy and jets; heavy-quarks, tau decay).

  The normal completion of the reconstruction task will result in a full set of these reconstructed objects usable in physics analyses. Reconstruction is expensive in terms of CPU and is dominated by tracking.

- AOD ("Analysis Object Data"): this is a "distilled" version of the RECO event information, and is expected to be used

for most analyses. AOD provides a compromise between event size and complexity of the available information to optimize flexibility and speed for analyses, most of the raw information of the detector are lost at this point.

The overall collection of software used in CMS is referred to as CMSSW, it is built around a Framework, an Event Data Model (EDM), and Services needed by the simulation, calibration and alignment, and reconstruction modules that process event data so that analysis can be performed. The primary goal of the Framework and EDM is to facilitate the development and deployment of reconstruction and analysis software.

The CMSSW event processing model consists of one executable, called cmsRun, and many plug-in modules which are managed by the Framework. All the code needed in the event processing (calibration, reconstruction algorithms, etc.) is contained in the modules. The same executable is used for both detector and Monte Carlo data.

The CMSSW executable, cmsRun, is configured at run time by the user's job-specific configuration file. This file tells cmsRun

- which data to use
- which modules to execute
- which parameter settings to use for each module
- what is the order or the executions of modules, called path
- how the events are filtered within each path and how the paths are connected to the output files

The CMS Event Data Model (EDM) is centered around the concept of an Event. An Event is a C++ object container for all RAW and reconstructed data related to a particular collision. During processing, data are passed from one module to the next via the Event, and are accessed only through the Event. All objects in the Event may be individually or collectively stored in ROOT files, and are thus directly browsable in ROOT.

Given the large data volumes involved and the large size of the CMS collaboration, a fully distributed computing model is used for data reconstruction and analysis. The system is based upon Grid middleware, with the common Grid services at centres defined and managed through the Worldwide LHC Computing Grid (WLCG) project, a collaboration between LHC experiments, computing centres, and middleware providers.

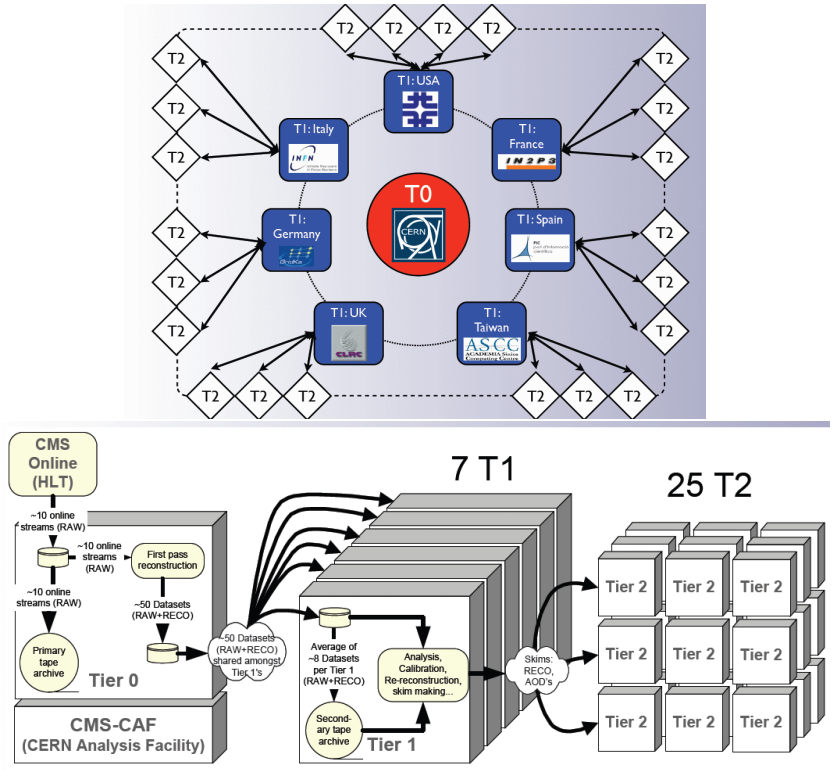

Figure 2.13.: Schematic representation of the CMS Grid storage tier structure and the associated data workflow

3 ANALYSIS

3.1 INTRODUCTION

Understanding quarkonium production in hadronic collisions is a serious challenge to QCD. Specifically, because of their feed-down contribution, understanding the production mechanism of the p-wave states χ_c (χ_b) is important when studying the polarization of promptly produced J/ψ (Υ). In that respect, measurements of the ratios of the prompt production cross sections of the quarkonium states are particularly interesting as they are very little affected by theoretical and experimental uncertainties. Nevertheless significant deviations from the value of the χ_{c2}/χ_{c1} production ratio expected from simple spin counting or color-singlet models were reported in the past by the CDF Collaboration [2]. A measurement of χ_{c2}/χ_{c1} production ratio was performed by the CMS experiment in proton-proton collisions on about 4.6 fb^{-1} of integrated luminosity collected at $\sqrt{s}$=7 TeV [10]. Within the uncertainties we observed a decrease of the χ_{c2}/χ_{c1} ratio at increasing values of $p_T(J/\psi)$ as reported by CDF [2] and LHCb [1] Collaborations, and comparisons with theoretical models are not conclusive.

The high luminosity delivered by the LHC in 2012 is a unique opportunity to extend the measurement of this ratio to the corresponding bottomonium states. In this analysis we present our measurement of the ratio

$$\mathcal{R} = \sigma(pp \to \chi_{b2} + X)/\sigma(pp \to \chi_{b1} + X)$$

in four different bins of p_T of the $\Upsilon(1S)$.

The strategy of the analysis is the following: The χ_{b1} and χ_{b2} states are reconstructed by searching for their radiative decay into the $\Upsilon(1S)$ plus photon final state, with the $\Upsilon(1S)$ decaying into two muons. The ratio of the production cross sections is then obtained as

$$\mathcal{R} = \frac{N_{\chi_{b2}}}{N_{\chi_{b1}}} \cdot \frac{\varepsilon_1}{\varepsilon_2} \cdot \frac{\mathcal{B}(\chi_{b1}(1P) \to \Upsilon(1S)\gamma)}{\mathcal{B}(\chi_{b2}(1P) \to \Upsilon(1S)\gamma)} \tag{3.1}$$

where $N_{\chi_{b1,2}}$ is the number of signal candidates of each type obtained from the dimuon-photon spectrum, $\varepsilon_1/\varepsilon_2$ is the efficiency correction obtained from a full detector simulation and

the branching ratios for radiative decays $\mathcal{B}(\chi_{b1,2}(1P) \to \Upsilon(1S)\gamma)$ are taken from the recent updates supplied by the PDG [6].

Because of the small difference between the masses of the χ_{b1} and of the χ_{b2}, 19.4 MeV, a calorimetric measurement of the photon energy would not provide sufficient resolution to disentangle the two states. Since the E_T of the detected photon in the laboratory mostly lies between 500 MeV and 2 GeV, a measurement of the momentum of the electron-positron pair, originating from a conversion of the photon in the beam pipe or in the inner layers of the tracker detector, results in a very accurate measurement of the photon energy. The drawback is the reduced yield due to the small probability for a conversion to occur in the innermost part of the tracker and, more importantly, the low reconstruction efficiency. To reduce the uncertainty due to the finite resolution of the reconstructed dimuon pair, event-by-event constraints on the dimuon-photon system have been developed. Background subtracted yields of χ_{b1} and χ_{b2} are then extracted simultaneously from an unbinned maximum likelihood fit to the invariant mass of the dimuon-photon system. Finally, a correction is applied to take into account the different acceptance of the detector for the two states.

3.2 DATA AND MONTE CARLO SAMPLES

The whole amount of proton-proton collisions collected in the 2012 a $\sqrt{s}$= 8 TeV was used for this analysis. This sample corresponds to an integrated luminosity of $20.7 \pm 0.9 fb^{-1}$.

The analysis relies on *Stream A* data, which in 2012 contained HLT trigger paths specifically designed for Υ selection. The trigger path we considered is `HLT_Dimuon7_Upsilon_v*`. This trigger requires that the minimum p_T of the Υ candidate is 7 GeV. Other requirements imposed at HLT include the request that dimuon candidates have an invariant mass between 8.5 GeV and 11.5 GeV, a distance of closest approach to the beam axis less than 5 mm and a χ^2 probability from the kinematical fit to a common vertex larger than 0.5%. Details about the datasets we used can be found in Table 3.1.

In order to determine the efficiency corrections, a Monte Carlo simulation sample of 40 millions of χ_{b1} and 40 millions of χ_{b2} was used. Similarly to the measurement of the χ_{c2}/χ_{c1} ratio, since the photon reconstruction efficiency is very low, of the order of 0.1% for photons with E_T= 1 GeV, the use of a full Monte Carlo is not viable because of the excessive amount of CPU time that would be required. The sample was instead produced with

Data samples	Run range
/MuOnia/Run2012A-13Jul2012-v1/AOD	190 456 — 193 621
/MuOnia/Run2012A-recover-06Aug2012-v1/AOD	190 782 — 190 949
/MuOnia/Run2012B-13Jul2012-v1/AOD	193 833 — 196 531
/MuOnia/Run2012C-24Aug2012-v1/AOD	198 022 — 198 913
/MuOnia/Run2012C-PromptReco-v2/AOD	198 934 — 203 746
/MuOnia/Run2012D-PromptReco-v1/AOD	203 768 — 208 686

Table 3.1.: CMS data samples used for the analysis.

a PYTHIA *particle gun* configured in such a way that the χ_{b1} and χ_{b2} particles are generated with the same p_T spectrum, chosen to be the one measured by the CMS experiment for the $\Upsilon(2S)$, limited to the range between 5 GeV and 50 GeV. The χ_{b1} and χ_{b2} were generated in the rapidity range $|y| < 2.0$. Both χ_b's were forced to decay to $\Upsilon(1S) + \gamma$. Only events in which a conversion occurred were retained and processed through the full CMS detector simulation, trigger selection and reconstruction. As explained in [4], in simulating the χ_b decay PYTHIA does not take into account the correct polarization of the Υ, which is made to decay isotropically in its rest frame. We applied a reweighting procedure to assign the correct angular distribution to Υ decays. Further details on the *particle gun* simulation are given in Section 3.4.

3.3 EVENT RECONSTRUCTION AND SELECTION

The candidate χ_b is the result of the muon selection, of the $\Upsilon(1S)$ selection, of the photon selection and of the requirements imposed on the relation between the photon candidate and the $\Upsilon(1S)$ candidate. Table 3.2 presents a summary of the cuts. In the following we describe the process in detail.

3.3.1 $\Upsilon(1S)$ reconstruction

The $\Upsilon(1S)$ selection starts with the standard CMS muon reconstruction. Muons are selected using POG-recommended quality criteria. Muon pairs are then considered and further cuts are applied.

Muon reconstruction

Standalone muon

The muon reconstruction chain starts with the local recon-

struction: hits in the muon system (drift tubes, cathode strip chambers, resistive plate chambers) are reconstructed from electronic signal, hits are then matched to form "segments". In the offline (i.e. after the data has been stored permanently) reconstruction these segments are used to generate seeds consisting of position and direction vectors which are fitted along with the other hits using a Kalman filter technique. The result of this fit is referred to as *standalone muon* as no information as been used from the inner tracking system.

Global muon

For each standalone muon track a matching with the tracks reconstructed in inner tracking system (tracker tracks) is then performed and the best-matching one is selected. A new fit based on the Kalman filter technique is performed using the hits of both the inner tracking and the muon system and its result is referred to as *global muon*. These object are optimized for muons with hight p_T, as the one used in Higgs and SUSY analyses, however low-p_T muons (with p_T of the order of several GeV) may not leave enough hits in the muon stations for a standalone muon to be reconstructed.

Tracker muon

For this reason a complementary approach as been developed: each tracker track is considered a potential muon candidate this hypothesis is checked by looking for a compatible signature in the calorimeters and the muon system. Tracker tracks identified as muons by this method are referred to as *tracker muons*. The criteria for tagging a track as tracker muon are loose ($p > 2.5\,\text{GeV}$, $p_T > 0.5\,\text{GeV}$ and a match with at least one segment in the muon stations) so additional quality cuts are required. To avoid double counting each track used to form a global muon cannot be tagged as tracker muon.

For the present analysis both global and tracker muons are used but in both cases the momentum is reconstruct from the tracker track as for low momentum muons the multiple scattering and showers traversing the magnet and the iron yoke can corrupt the measurement of the muon trajectory.

Muon selection

For this analysis we use *Global* or *Tracker* muons with the PAG recommended *Soft Muons* selection. Muon identification is achieved requiring the tracker track to be matched with at least one muon segment, in any station, both in x and y coordinates (`TMOneStationTight`). To ensure an accurate p_T measurement and suppress decays in flight, the number of tracker layers with at least one hit must be greater than five, at least one hit being in the pixel detector. The reduced χ^2 of the track fit must be less

than 1.8. Loose cuts are applied to the transverse and longitudinal impact parameter, $d_{xy} < 3$ cm and $d_z < 30$ cm respectively, to suppress decays in flight and cosmic muons.

Dimuon selection

Each pair of opposite sign muons is taken into account and is considered a Υ candidate if:

- its invariant mass is between 8.5 GeV and 11 GeV,
- the absolute value of its rapidity is less than 1.25,
- the χ^2 probability of a fit where the two muon tracks are constrained to a common vertex is more than 1%.

To select muon pairs originating from the decay of the $\Upsilon(1S)$, we ask the dimuon mass to be within 2.5 σ from the $\Upsilon(1S)$ pole mass where, following reference [12], the resolution σ is parameterized as a function of y_Υ, the rapidity of the Υ, as:

$$\sigma/\,\mathrm{GeV} = 0.058 + 0.047 \cdot (|y_\Upsilon| - 0.22).$$

3.3.2 Photon reconstruction

Photon conversions are characterized by an electron-positron pair originating from the photon conversion vertex. Because of the energy spectrum of the photon from the radiative decay, the electron and positron tracks are low-p_T tracks. In addition the tracks can be very asymmetric, with one of the two leptons carrying most of the photon energy. For these reasons the majority of the leptons are fully stopped before reaching the calorimeter or bent in spirals inside the tracking detector. An algorithm which uses only tracker information is then needed to reconstruct them.

To efficiently reconstruct low-p_T and displaced tracks as those coming from a typical photon conversion, the algorithm relies on the capability of iterative tracking as described in [26].

Selection

For this analysis only standard *high quality* conversions reconstructed from *general tracks* are used. The *high quality* requirement consists of the follwing:

- the two tracks must have at least two and four hits in the tracker,
- the reduced χ^2 of their track fit must be less than 10,

- the χ^2 probability of the kinematic fit to a common vertex must be more than $5 \cdot 10^{-4}$,
- the two tracks should be almost parallel with a small angular separation $\Delta\phi < 0.2$ and $\Delta(\cot\vartheta) < 0.1$.

Because of the magnetic field generated by the solenoid, the two tracks are expected to open in the transverse plane with two possible orientations: *seagull* (electrons bent apart) and *cowboys* (electrons bent together). Two additional cuts are then applied to select *seagull* events: $-0.25 \text{ cm} < d_m < 1 \text{ cm}$ where $d_m = d_{O_1-O_2} - (R_1 - R_2)$ is the distance of minimum approach and $d_0 \cdot q > 0$.

For the purpose of this analysis an additional selection is applied requiring the vertex of the conversion to be at least 1.5 cm away from the beam direction in order to suppress Dalitz decays of the π^0.

3.3.3 χ_b reconstruction

For each event the selected $\Upsilon(1S)$ candidates and the converted photons are paired to form χ_b candidates. The d_z of the photon with respect to the dimuon vertex, i.e. the distance in the direction parallel to the z axis between the dimuon vertex and the extrapolation of the photon direction to the beamline, is required to be less than 1 mm and the per-event mass difference, or Q-value $Q = m_{\mu\mu\gamma} - m_{\mu\mu}$, must be less than 2 GeV.

To reduce the event-by-event fluctuations due to the finite resolution on the reconstructed mass of the dimuon, two strategies have been developed and applied to build the spectra of the χ_b candidates:

- a kinematic fit of the muons and electron-positron tracks,
- the use of the per-event mass difference Q.

As the first method provides a better signal over background ratio, the reference results are computed from a fit to the spectrum of the $\mu\mu\gamma$ invariant mass after the kinematic fit, referred to as $m(\chi_b)$ in the following. Alternatively distributions of the Q-value are used for consistency checks.

Kinematic fit

The kinematic fit is performed imposing the following constraints:

- the masses of muons and electrons are bound to the physical masses;
- the mass of the dimuon is constrained to the nominal mass of $\Upsilon(1S)$;
- the mass of the electron-positron pair is constrained to zero;
- the two electrons are supposed to have a common vertex;
- the two muons and the photon are constrained to have a common vertex.

χ_b candidates are retained if the χ^2 probability of the kinematic fit is more than 0.02.

3.4 SIGNAL MODEL

The reconstructed $m(\chi_b)$ shape is parameterized using the *particle gun* simulation described in Section 3.2. The intrinsic width of the χ_b states is not measured, but we assume it to be negligible in comparison to the resolution of the detector, which is of the order of 5 MeV. This assumption is supported by the fact that, as we will see in the following, the lineshape of the detector response fits well the experimental distribution. The observed signal shape is therefore dominated by the detector resolution.

The invariant mass resolution, dominated by the energy resolution of the converted photon, is sufficient to separate the χ_{b1} and χ_{b2} peaks. The resolution function presents a low-energy tail, typical of processes in which radiative losses play a role, as in the case of electrons from converted photons loosing energy in the tracking detector. Since the tail of the χ_{b2} falls under the χ_{b1} peak, it is important to obtain a reliable parameterization of the resolution function in order to achieve an unbiased estimation of the ratio $N_{\chi_{b2}}/N_{\chi_{b1}}$. To empirically model processes in which radiative losses are involved, the Crystal Ball function [29] is frequently used. It is composed of a Gaussian core, described by the two parameters m and σ_{CB}, and a power-law low energy tail described by other two parameters, α, the transition point between Gaussian and exponential, and n, the index of the power-law tail. The Crystal Ball function allows to describe the Gaussian component representing the detector resolution, as well as the component corresponding to un-recovered energy losses by means of the power-law tail. Simulations show that, in the signal shape, a small high-energy tail is also present.

Table 3.2.: Summary of the selection requirements used to select χ_b candidates.

MUON AND DIMUON SELECTION	
track fit χ^2/ndof	<1.8
hits in Pixel	$\geqslant 1$
hits in Tracker	$\geqslant 5$
Fiducial cylinder	3 cm (r) $\times$ 30 cm (z)
$\mu\mu$ vertex fit probability	>0.01
Muon id	`TMuonOneStationTight`
$m_{\mu\mu}$	8.5 - 11 GeV
$\lvert\eta(\mu\mu)\rvert$	< 1.25
PHOTON CONVERSION SELECTION	
Electron track hits	$\geqslant 4, 2$
Electron track fit χ^2/ndof	< 10
Distance of approach	-0.25cm $< d_m <$ 1cm
Signed impact parameter	$q \cdot d_0 > 0$
e^+e^- vertex fit probability	$> 5 \times 10^{-4}$
Radius of conversion	$R_{conv} > 1.5$ cm
$\Delta\phi(e^+e^-)$	< 0.2
$\Delta\left(\cot\vartheta(e^+e^-)\right)$	< 0.1
$\lvert\eta(\gamma)\rvert$	< 1.0
χ_b SELECTION	
$m_{\mu\mu\gamma} - m_{\mu\mu}$	< 2 GeV
$dz(\Upsilon\gamma)$	< 1 mm
$\lvert m_{\mu\mu} - m_\gamma\rvert$	$< 2.5\,\sigma$
Probability of kinematic fit	> 0.02

Therefore we choose to parametrize our resolution function with a double-sided Crystal Ball function, which is composed of both a high-energy and low-energy power-law tail, with independent exponents and transition points, but with a common Gaussian core. As the α and n parameters are strongly correlated, we choose to fix n for both tails when fitting the Monte Carlo.

Previous studies [4] show that, in general, the resolution degrades with increasing transverse momentum of the Υ. This effect has to be attributed to the fact that, for higher p_T (Υ), the photon also is expected to have a higher transverse momentum and therefore is measured with less precision, because of the constant behavior of $\Delta p/p$ for charged particles of small energy measured in the Tracker. The present analysis, however, does not seem to highlight this feature, within statistical errors, in the p_T (Υ) range under examination.

The results of the fits are shown in Figures 3.2 and 3.3 and the parameters summarized in Table 3.3. The χ_{b1} mass we extract is about 4 MeV lower that the PDG value. This effect reproduces well the data, and it is attributed to the incomplete recovery of bremsstrahlung radiation emitted by the two electrons originating from the conversion candidate.

The variation of the fit parameters with Υ transverse momentum is represented in Figure 3.1.

Table 3.3.: Summary of the parameters from the fit to the simulated invariant mass distribution of the $\mu\mu\gamma$ system after the kinematic refit in the four p_T bins of the $\Upsilon(1S)$. Fit parameters are described in the text. The errors are the statistical uncertainty due to the finite size of the simulated samples.

	$p_T(\Upsilon)$ [GeV]	m [GeV]	σ [GeV]	α_1	α_2	$\chi^2/ndof$
χ_{b1}	7 - 11	9.8892 ± 0.0003	0.0057 ± 0.0003	0.73 ± 0.04	1.54 ± 0.09	0.62
	11 - 16	9.8885 ± 0.0003	0.0061 ± 0.0003	0.77 ± 0.04	1.8 ± 0.1	0.42
	16 - 20	9.8885 ± 0.0005	0.0058 ± 0.0005	0.71 ± 0.06	1.9 ± 0.2	0.27
	20 - 40	9.8875 ± 0.0003	0.0055 ± 0.0003	0.67 ± 0.04	1.9 ± 0.1	0.54
χ_{b2}	7 - 11	9.9094 ± 0.0004	0.0063 ± 0.0005	0.83 ± 0.06	1.5 ± 0.1	0.5
	11 - 16	9.9093 ± 0.0004	0.0059 ± 0.0004	0.72 ± 0.05	1.56 ± 0.09	0.4
	16 - 20	9.9075 ± 0.0005	0.0068 ± 0.0004	0.89 ± 0.07	2.2 ± 0.2	0.33
	20 - 40	9.9087 ± 0.0004	0.0058 ± 0.0004	0.61 ± 0.04	1.9 ± 0.2	0.74

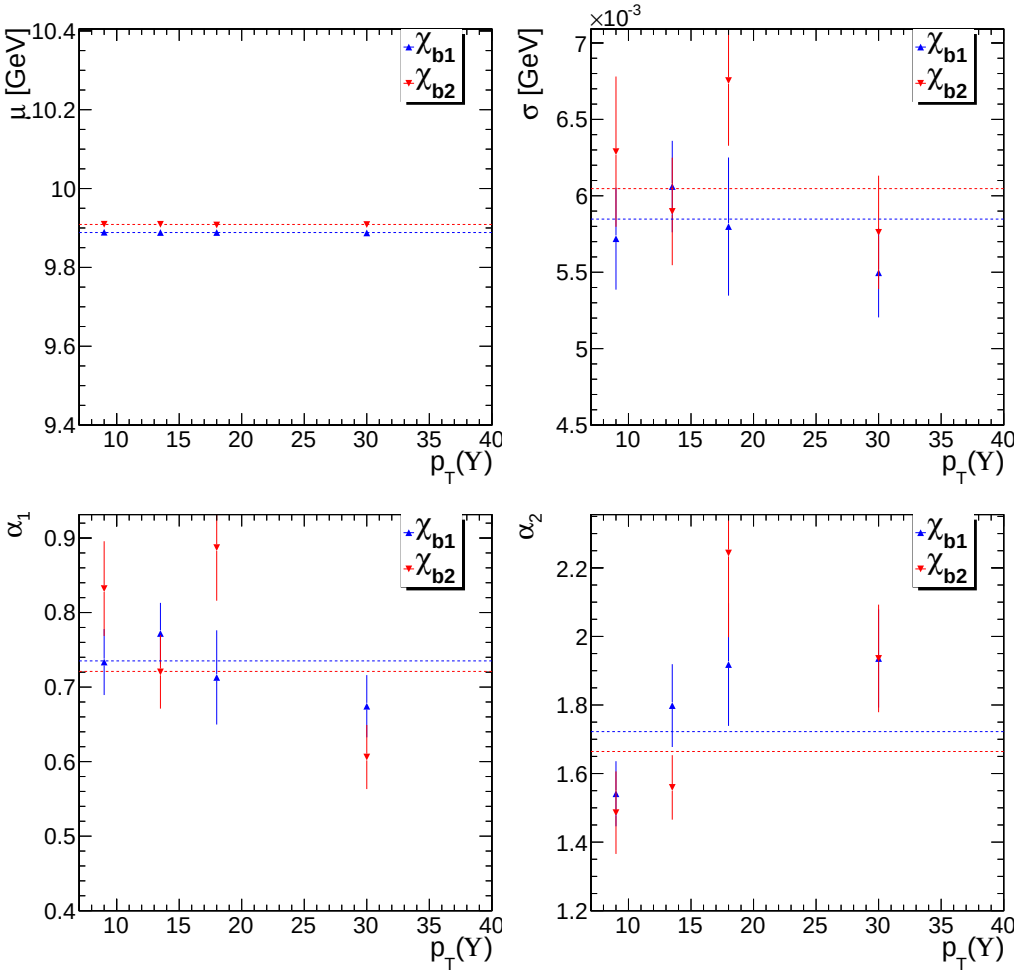

Figure 3.1.: Fitted parameters as a function of the bin of p_T (Υ). The solid lines represent the values from the fit on the full p_T range.

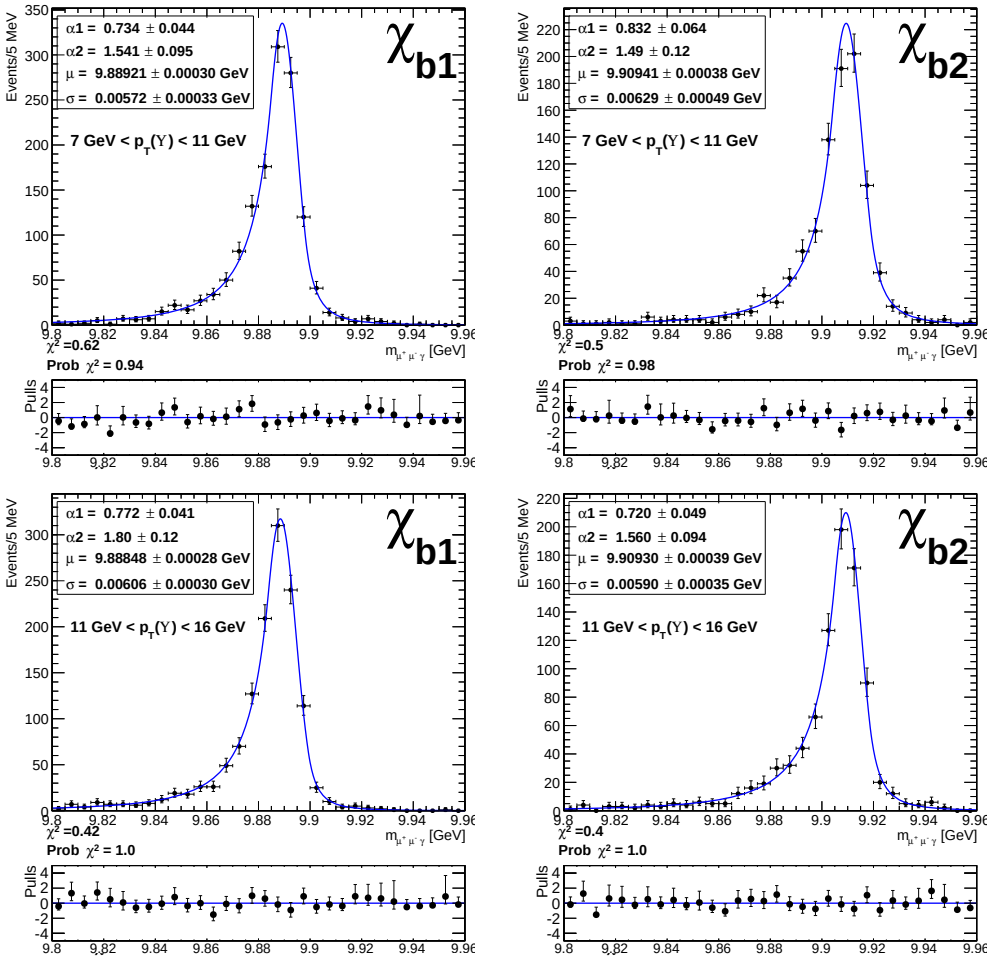

Figure 3.2.: Invariant mass distribution of the $\mu\mu\gamma$ system after the kinematic refit in the two lowest p_T bins of the $\Upsilon(1S)$ in simulated events. Signal is fitted the double-sided Crystal Ball described in the text. Signal shapes for χ_{b1} and χ_{b2} are shown separately.

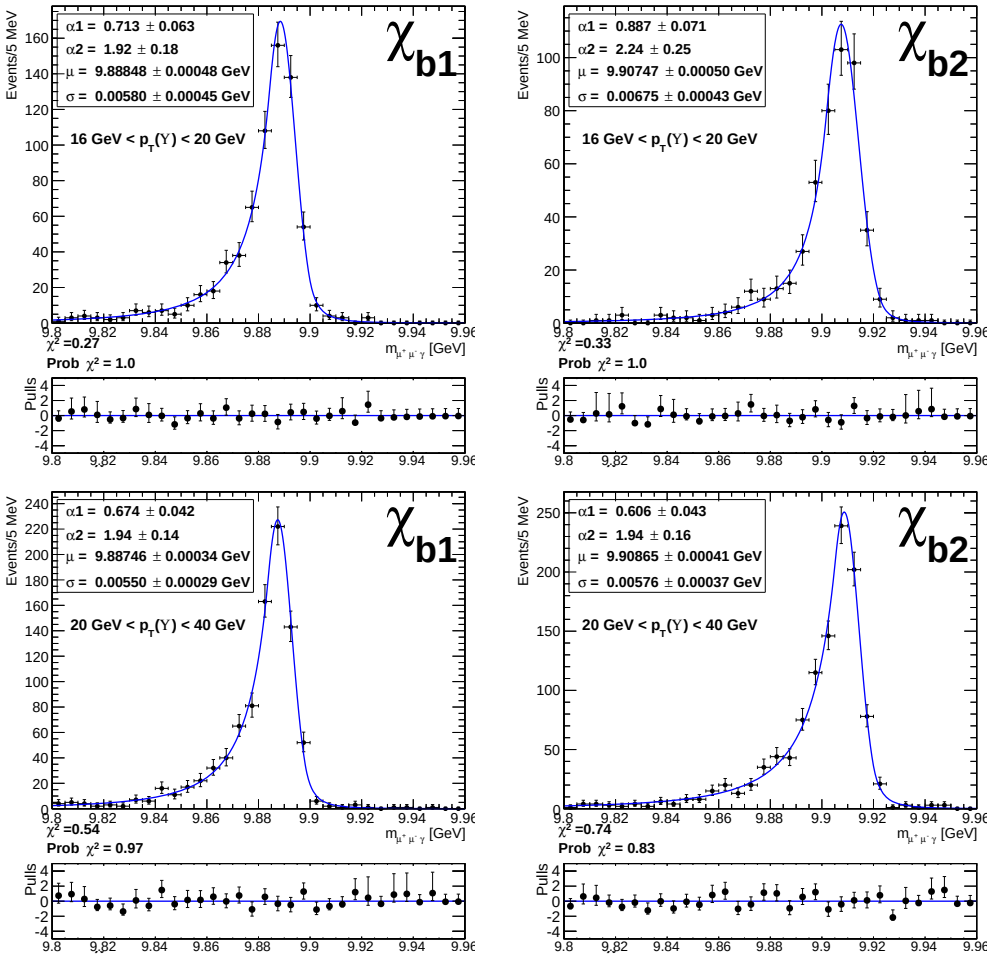

Figure 3.3.: Invariant mass distribution of the $\mu\mu\gamma$ system after the kinematic refit in the two highest p_T bins of the $\Upsilon(1S)$ in simulated events. Signal is fitted with the double-sided Crystal Ball described in the text. Signal shapes for χ_{b1} and χ_{b2} are shown separately.

3.5 SIGNAL EXTRACTION

We extract the ratio of χ_{b2} and χ_{b1} events, $N_{\chi_{b2}}/N_{\chi_{b1}}$, from the data by performing an unbinned maximum-likelihood fit to the $m(\chi_b)$ spectrum in ranges of Υ transverse momentum.

The probability density function for the signal is derived from the simulation as described above, and is modeled by the superposition of two double-sided Crystal Ball functions for the χ_{b1} and χ_{b2}. When fitting the data, we fix all the parameters of the Crystal Ball function to the values that best fit the simulation and use a maximum-likelihood approach to derive $N_{\chi_{b2}}/N_{\chi_{b1}}$ and the total number of χ_b candidates.

The background is modeled by a probability distribution function defined as

$$F_{bkg}(m) = (m - m_0)^{\lambda} \cdot e^{\nu(m-m_0)},$$

where m is the $\mu\mu\gamma$ invariant mass obtained after the kinematical fit, m_0, λ and ν are free parameters. The final likelihood function reads:

$$P(m) = N_{sig}\,[f_1 \cdot F_1(m) + (1 - f_1) \cdot F_2(m)] + N_{bkg} \cdot F_{bkg}(m),$$

where N_{sig} is the total number of χ_{b1} and χ_{b2} candidates, f_1 is the fraction of χ_{b1}, N_{bkg} is the total number of background events, F_1 and F_2 are the double-sided Crystal-Ball functions that describe the detector response for the two resonances. Invariant mass distributions in the data together with the fitted signal shapes are shown in Figure 3.4. Table 3.4 shows the results of the fit, as well as the total number of χ_{b1} and χ_{b2}.

Table 3.4.: Summary of the parameters from the fit to the data invariant mass distribution of the $\mu\mu\gamma$ system after the kinematic refit in the four p_T bins of the $\Upsilon(1S)$. Fit parameters are described in the text. The errors are the statistical uncertainty due to the finite size of the samples.

$p_T(\Upsilon)$ [GeV]	7 - 11	11 - 16	16 - 20	20 - 40
$N_{\chi_{b1}}$	420 ± 40	660 ± 40	350 ± 30	460 ± 30
$N_{\chi_{b2}}$	280 ± 40	360 ± 30	200 ± 20	320 ± 30
$N_{\chi_{b2}}/N_{\chi_{b1}}$	0.66 ± 0.11	0.549 ± 0.067	0.571 ± 0.082	0.701 ± 0.084
N_{bkg}	6630 ± 90	4130 ± 70	1370 ± 40	1440 ± 40
m_0 [GeV]	9.52 ± 0.02	9.5 ± 0.2	9.5 ± 0.2	9.5 ± 0.2
λ	3.2 ± 0.4	1.9 ± 0.8	0.2 ± 0.6	0.4 ± 0.6
ν [GeV^{-1}]	-5.7 ± 0.8	-4 ± 1	-0.0 ± 0.5	-2 ± 2
$\chi^2/ndof$	0.93	0.91	0.71	0.78

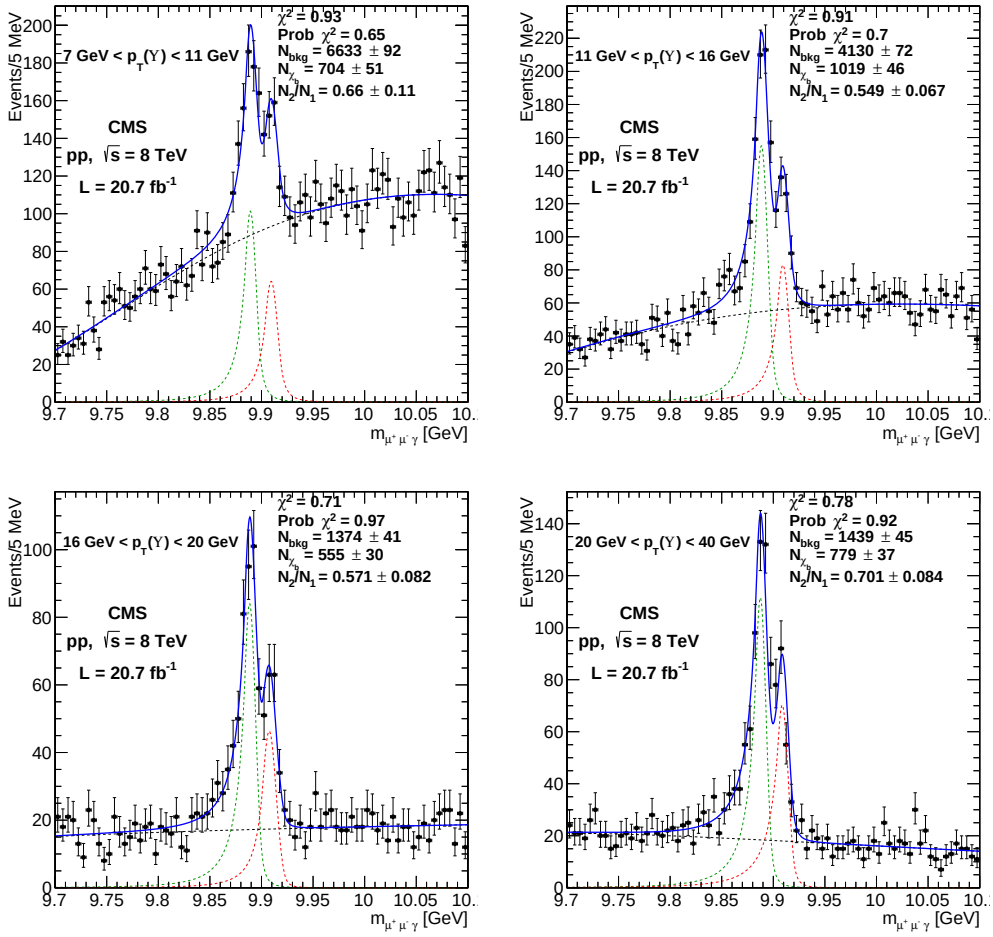

Figure 3.4.: Invariant mass distribution of the $\mu\mu\gamma$ system after the kinematic refit in the four p_T bins of the $\Upsilon(1S)$ in data. The shapes of the χ_{b1} and χ_{b2} signals, green and red dashed curves respectively, are parameterized with the double-sided Crystal Ball determined using simulated events.

Table 3.5.: Fractional systematic uncertainties on $N_{\chi_{b2}}/N_{\chi_{b1}}$ for different ranges of $\Upsilon(1S)$ transverse momentum from different sources and the total uncertainty.

$p_T(\Upsilon)$ [GeV]	7 - 11	11 - 16	16 - 20	20 - 40
Source of uncertainty	Systematic uncertainty (%)			
Signal parameterization	2.8	3.5	4.7	4.1
Choice of χ_b p_T spectrum	0.1	0.1	0.1	0.2
Statistical error on $\varepsilon_1/\varepsilon_2$	4.2	4.3	5.9	4.4
Total uncertainty	5.0	5.5	7.5	6.0
Statistical error	17.3	12.2	14.4	12.0

3.6 SYSTEMATIC ERRORS

Several types of systematic uncertainties are addressed. In particular, we investigate possible effects that could influence the measurement of the numbers of signal χ_{b1} and χ_{b2} from data, the evaluation of $\varepsilon_1/\varepsilon_2$ from the simulation, and the extraction of $N_{\chi_{b2}}/N_{\chi_{b1}}$. In Table 3.5 the various sources of systematic uncertainties and their contributions to the total uncertainty are summarized. The following subsections describe how the various contributions are evaluated.

3.6.1 Uncertainty from the mass fit and χ_{b1} and χ_{b2} counting

In counting the number of signal χ_{b1} and χ_{b2}, we take into account the fact that our signal model is extracted from a Monte Carlo with finite statistics. Therefore the parameters of the model are determined with a sizeable error. To estimate the impact of this uncertainty on the measurement of $N_{\chi_{b2}}/N_{\chi_{b1}}$, we perform several pseudo-experiments, in which a set of parameters is drawn randomly using the error matrix supplied by RooFit [31]. These parameters are then used to fit the data and extract a value of $N_{\chi_{b2}}/N_{\chi_{b1}}$ for each randomly-drawn set of parameters. The result of the pseudo-experiments for each rapidity bin is shown in Figure 3.5. The observed distribution of $N_{\chi_{b2}}/N_{\chi_{b1}}$ is fitted with a Gaussian function, and the standard deviation of the Gaussian taken as a systematic error for that rapidity bin.

The above procedure takes into account the uncertainty stemming from the imperfect parameterization of the Monte Carlo signal shape, where the Monte Carlo is assumed to perfectly re-

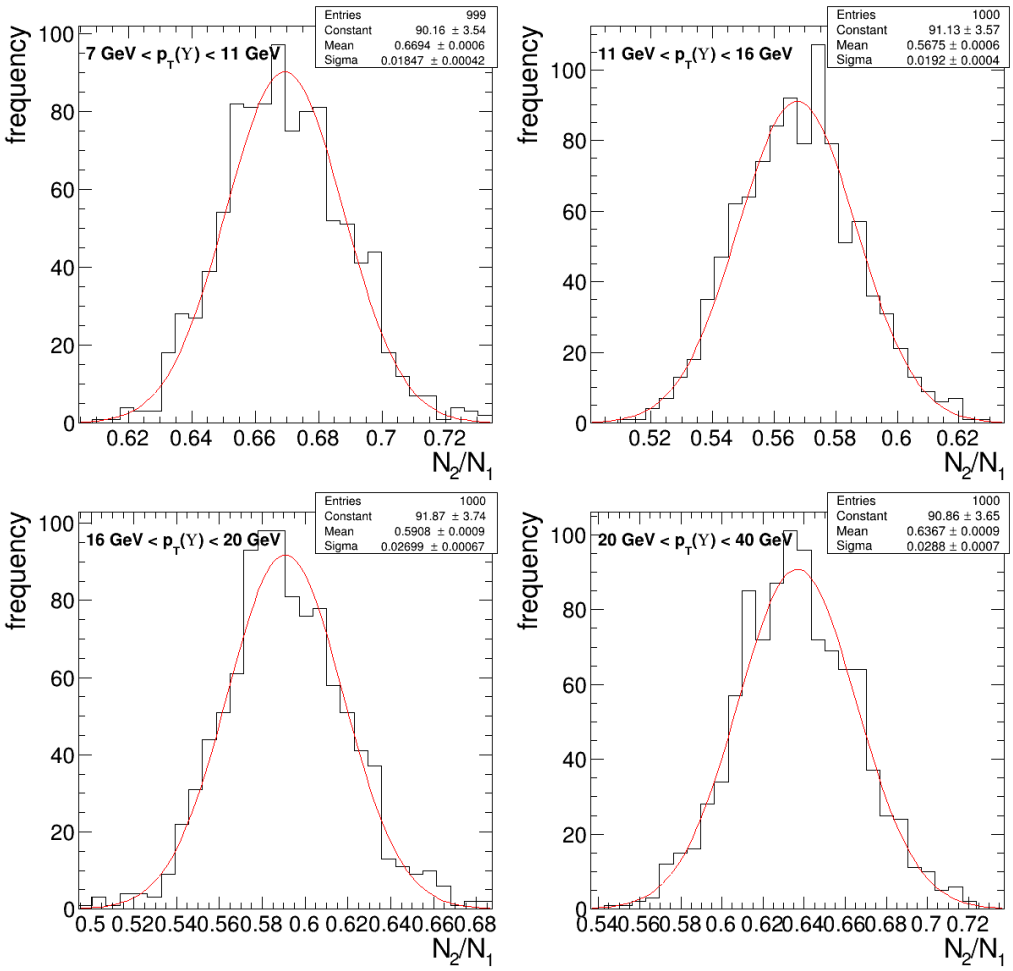

Figure 3.5.: Distribution of $N_{\chi b2}/N_{\chi b1}$ when the parameterization of the signal is varied randomly using the error matrix (see text). The distributions refer to the four p_T (Υ) bins.

produce reality. As a further check, we use an alternative fitting scheme with an increased number of free parameters, to take into account:

1. possible discrepancies in the energy scale between data and Monte Carlo;
2. possible discrepancies in the experimental resolution between data and Monte Carlo;
3. variations of the result with the choice of background model.

To address the first point, we allow the value of the mass of the χ_{b1} to fluctuate, while keeping the difference between the masses of the χ_{b1} and χ_{b2} fixed. Similarly, to address the second possibility, we allow the σ of the Crystal Ball function that describes the χ_{b1} to vary, while keeping the σ for the χ_{b2} connected to the σ of the χ_{b1} by a scale factor. The dependency of the result with respect to the choice of background parameterization is studied by using a third-order Chebyshev polynomial as an alternative parameterization. Table 3.6 summarizes the results for each fitting strategy. The full set of fitted spectra can be found in Appendix A.

Table 3.6.: Results of the fits for the alternative fitting strategies described in the text.

$p_T(\Upsilon)$ [GeV]	7 - 11	11 - 16	16 - 20	20 - 40
Fitting strategy	N_2/N_1			
Default	0.67 ± 0.12	0.575 ± 0.071	0.570 ± 0.083	0.638 ± 0.075
Alternative signal	0.70 ± 0.12	0.489 ± 0.063	0.553 ± 0.082	0.636 ± 0.075
Alternative background	0.68 ± 0.12	0.574 ± 0.071	0.571 ± 0.083	0.636 ± 0.075
Alternative signal and background	0.71 ± 0.12	0.491 ± 0.063	0.554 ± 0.081	0.634 ± 0.075

In no case the variation from the default fitting strategy is statistically significant. We therefore choose not to assign a systematic uncertainty.

3.6.2 Uncertainty on the ratio of efficiencies

We investigated the sources of systematic uncertainties in the evaluation of $\varepsilon_1/\varepsilon_2$. The statistical uncertainty on the measurement of $\varepsilon_1/\varepsilon_2$ from the simulation, owing to the finite size of the Monte Carlo sample, is taken as a systematic uncertainty, as shown in Table 3.5.

In the *particle gun* simulation, we assumed that the χ_{b1} and χ_{b2} are produced with the p_T spectrum of the $\Upsilon(2S)$. We justify this choice in Section 3.8. In order to estimate the impact of this choice on the estimation of $\varepsilon_1/\varepsilon_2$, we compare the value of $\varepsilon_1/\varepsilon_2$ measured from this choice of p_T spectrum with a few different hypotheses.

Possible dependencies on the determination of $\varepsilon_1/\varepsilon_2$ on the description of the material budget in the Monte Carlo simulation were addressed in [4] and found to be negligible.

3.6.3 Pile up

As already done in [4], we study the possible dependence of the measurement from pile up. To do so, we divide our data in bins with different number of primary vertices reconstructed in the event. The results are shown in Figure 3.6. We do not observe a statistically significant dependence of the result, therefore we do not assign a systematic uncertainty.

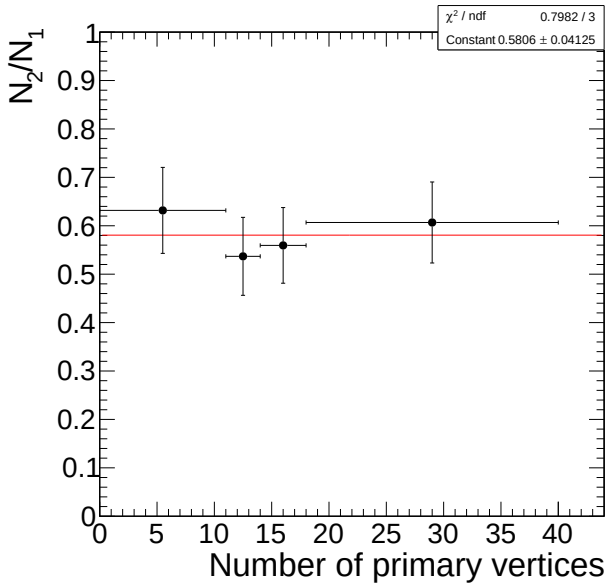

Figure 3.6.: Value of the fitted $N_{\chi_{b2}}/N_{\chi_{b1}}$ plotted as a function of the number of primary vertices reconstructed in the event. The solid line represents the value from the fit on the full sample on the full p_T range.

3.6.4 Branching fractions

The measurement of the χ_{b2} to χ_{b1} production cross section ratio is affected by the uncertainties on the branching fractions

of the two states into $\Upsilon(1S) + \gamma$. The quantity that is directly accessible in this analysis is $\frac{N_{\chi_{b2}}}{N_{\chi_{b1}}} \cdot \frac{\varepsilon_1}{\varepsilon_2}$ In order to extract $\mathcal{R}$, we use the value of $\mathcal{B}(\chi_{b1} \to \Upsilon(1S)\gamma)/\mathcal{B}(\chi_{b2} \to \Upsilon(1S)\gamma)$ as derived from the branching fractions and associated uncertainties reported in Ref. [6].

3.7 POLARIZATION

In estimating the ratio of efficiencies $\varepsilon_1/\varepsilon_2$ we have assumed that both the χ_{b1} and χ_{b2} are unpolarized. Polarization affects the angular distribution and the transverse momentum distribution of the photon. Because the photon reconstruction efficiency is varying rapidly as a function of photon transverse momentum, especially in the softer region, the ratio of efficiencies can change for different polarization scenarios. More details are explained in [4].

In order to investigate this effect, we reweight the unpolarized Monte Carlo distributions to reproduce the theoretical χ_b angular distributions [23] for different χ_b polarizations. We measure the efficiency $\varepsilon_1/\varepsilon_2$ for the χ_{b1} being unpolarized or with helicity $m_{\chi_{b1}} = 0, \pm 1$, in combination with the χ_{b2} being unpolarized or having helicity $m_{\chi_{b2}} = 0, \pm 1, \pm 2$ in both the helicity and Collins–Soper [20] frames. Tables 3.7 and 3.8 give the resulting $\varepsilon_1/\varepsilon_2$ values for each polarization scenario in different Υ transverse momentum bins for the two frames, relative to the value of the ratio for the unpolarized case. These tables, therefore, provide the correction that should be applied to the default value of $\varepsilon_1/\varepsilon_2$ in each polarization scenario and each range of transverse momentum.

3.8 SPECTRA OF KINEMATIC VARIABLES

To some extent, the ratio of efficiencies $\varepsilon_1/\varepsilon_2$ is affected by the production p_T spectra of the χ_{b1} and of the χ_{b2} which are unknown. Therefore we chose to explore different models for the χ_b spectra while using the data as a guide to make a reasonable assumption, and treat residual discrepancies as systematic uncertainties. Specifically we have studied the kinematical observables of the dimuon and of the photon for the selected χ_b candidates to elucidate what are the factors that are to be taken into account for understanding $\varepsilon_1/\varepsilon_2$ as a function of p_T (Υ).

Table 3.7.: The efficiency ratio $\varepsilon_1/\varepsilon_2$ for different polarization scenarios in which the χ_{b1} is either unpolarized or has helicity $m_{\chi_{cb}} = 0, \pm 1$ and the χ_{b2} is either unpolarized or has helicity $m_{\chi_{b2}} = 0, \pm 1, \pm 2$ in the helicity frame, relative to the unpolarized case.

Polarization scenario ($m_{\chi_{b1}}$, $m_{\chi_{b2}}$)	$p_T(\Upsilon)$ [GeV] 7 - 11	11 - 16	16 - 20	20 - 40	7 - 40
(Unpol., 0)	0.908 ± 0.010	0.901 ± 0.010	0.901 ± 0.013	0.915 ± 0.008	0.905 ± 0.005
(Unpol., ± 1)	0.932 ± 0.003	0.942 ± 0.004	0.960 ± 0.006	0.954 ± 0.004	0.943 ± 0.002
(Unpol., ± 2)	1.139 ± 0.009	1.130 ± 0.010	1.107 ± 0.013	1.105 ± 0.008	1.125 ± 0.005
(0, Unpol.)	0.867 ± 0.007	0.875 ± 0.007	0.903 ± 0.011	0.904 ± 0.009	0.879 ± 0.004
(0, 0)	0.787 ± 0.010	0.788 ± 0.011	0.814 ± 0.015	0.827 ± 0.011	0.795 ± 0.006
(0, ± 1)	0.808 ± 0.007	0.824 ± 0.008	0.867 ± 0.011	0.863 ± 0.010	0.829 ± 0.004
(0, ± 2)	0.987 ± 0.011	0.989 ± 0.012	1.000 ± 0.017	0.999 ± 0.013	0.988 ± 0.006
(± 1, Unpol.)	1.068 ± 0.003	1.063 ± 0.004	1.048 ± 0.005	1.048 ± 0.005	1.061 ± 0.002
(± 1, 0)	0.969 ± 0.011	0.958 ± 0.011	0.944 ± 0.015	0.958 ± 0.010	0.960 ± 0.006
(± 1, ± 1)	0.995 ± 0.005	1.001 ± 0.005	1.007 ± 0.008	1.000 ± 0.006	1.001 ± 0.003
(± 1, ± 2)	1.216 ± 0.010	1.202 ± 0.011	1.160 ± 0.015	1.158 ± 0.010	1.194 ± 0.006

Table 3.8.: The efficiency ratio $\varepsilon_1/\varepsilon_2$ for different polarization scenarios in which the χ_{b1} is either unpolarized or has helicity $m_{\chi_{cb}} = 0, \pm 1$ and the χ_{b2} is either unpolarized or has helicity $m_{\chi_{b2}} = 0, \pm 1, \pm 2$ in the Collins–Soper frame, relative to the unpolarized case.

Polarization scenario ($m_{\chi_{b1}}$, $m_{\chi_{b2}}$)	$p_T(\Upsilon)$ [GeV] 7 - 11	11 - 16	16 - 20	20 - 40	7 - 40
(Unpol., 0)	0.997 ± 0.011	1.018 ± 0.012	1.014 ± 0.017	1.035 ± 0.011	1.030 ± 0.007
(Unpol., ± 1)	0.975 ± 0.005	0.997 ± 0.006	1.001 ± 0.009	1.010 ± 0.006	1.001 ± 0.003
(Unpol., ± 2)	1.029 ± 0.009	0.993 ± 0.010	0.991 ± 0.014	0.974 ± 0.008	0.984 ± 0.005
(0, Unpol.)	0.980 ± 0.008	1.009 ± 0.009	1.020 ± 0.013	1.042 ± 0.012	1.020 ± 0.005
(0, 0)	0.977 ± 0.014	1.028 ± 0.015	1.035 ± 0.021	1.078 ± 0.017	1.051 ± 0.009
(0, ± 1)	0.956 ± 0.009	1.007 ± 0.011	1.022 ± 0.016	1.052 ± 0.014	1.022 ± 0.006
(0, ± 2)	1.009 ± 0.012	1.003 ± 0.013	1.011 ± 0.019	1.014 ± 0.015	1.004 ± 0.007
(± 1, Unpol.)	1.009 ± 0.004	0.995 ± 0.004	0.990 ± 0.006	0.979 ± 0.006	0.990 ± 0.003
(± 1, 0)	1.006 ± 0.012	1.013 ± 0.013	1.004 ± 0.018	1.013 ± 0.013	1.020 ± 0.007
(± 1, ± 1)	0.985 ± 0.006	0.993 ± 0.008	0.992 ± 0.011	0.989 ± 0.009	0.991 ± 0.004
(± 1, ± 2)	1.039 ± 0.010	0.989 ± 0.011	0.982 ± 0.015	0.954 ± 0.010	0.974 ± 0.006

These studies take advantage of data and Monte Carlo comparisons performed with the help of a background subtraction procedure. Three ranges of $m_{\mu^+\mu^-\gamma}$ are defined: a left side band [9.70,9.87] GeV (*LB*), the signal region [9.87, 9.92] GeV (*SR*) and a right side band [9.92,10.10] GeV (*RB*). The fraction of background events in the signal region (f_{BG}) is estimated from the fit to the data. The histograms of the spectrum of the desired kinematic variables in the three mass ranges are produced. The distribution of background events (*BG*) is modeled by averaging the distributions in the two side bands, taken with the same weight. Background-subtracted distributions are finally produced by subtracting, from the distributions in the signal region, the background distributions, normalized to the fraction of background estimated in the signal region, as in the following :

$$SR_i^* = SR_i - f_{BG} \cdot (\sum_j SR_j) \cdot \frac{BG_i}{\sum_j BG_j}$$

where SR_i^* is the content of the i^{th} bin of the background subtracted distribution, and j runs over all the bins.

The *particle gun* Monte Carlo was produced using as χ_b production p_T spectrum a parameterization of the $\Upsilon(2S)$ production spectrum measured by CMS [11]. The efficiency-corrected observed p_T spectrum of $\Upsilon(2S)$ has been parameterized as:

$$\frac{dN}{dp_T} \propto p_T \left[1 + \frac{1}{(\beta - 2)} \frac{p_T^2}{< p_T^2 >}\right]^{-\beta}, \tag{3.2}$$

where β and $< p_T^2 >$ are free parameters that change for each resonance. The values of these parameters used in this analysis are reported in Table 3.9.

Table 3.9.: Parameters describing the p_T spectra of the $\Upsilon(1S)$, $\Upsilon(2S)$ and $\Upsilon(3S)$ resonances.

Resonance	β	$< p_T^2 >$ [GeV^2]
Υ (1S)	3.24 ± 0.11	51.0 ± 1.2
Υ (2S)	2.84 ± 0.16	75.0 ± 4.3
Υ (3S)	3.31 ± 0.55	75.4 ± 6.2

Event reweighting was used to explore the $\Upsilon(1S)$ hypothesis. The resulting distributions for the p_T of the $\Upsilon(1S)$ and for the E_T of the photon are shown in Figures 3.7 and 3.8, for the case in which the χ_b in the *particle gun* simulation are produced following the measured $\Upsilon(2S)$ and $\Upsilon(1S)$ respectively. The data-Monte

Carlo agreement for both variables is best when the $\Upsilon(2S)$ spectrum is used. This is in agreement with naive expectations, since the $\Upsilon(2S)$ is the bottomonium state closest in mass to the χ_b (1P).

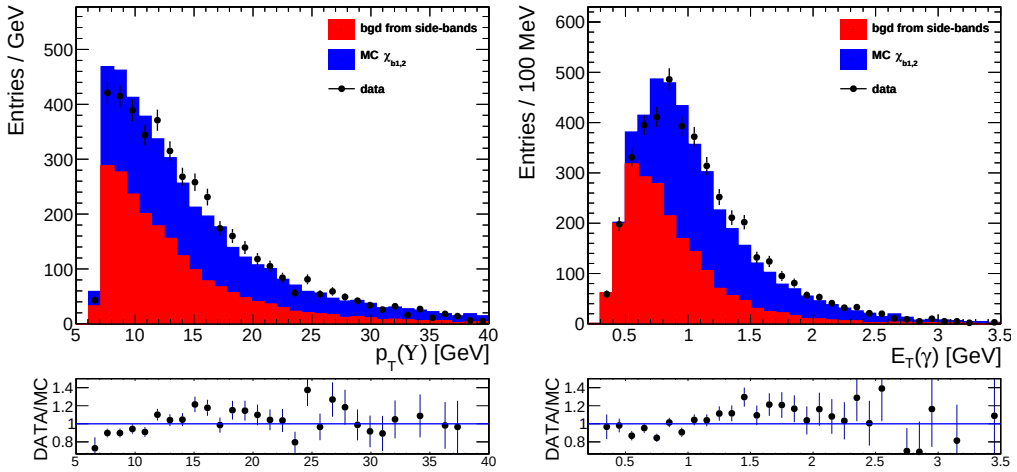

Figure 3.7.: Comparison of Monte Carlo and data spectra when the input p_T (χ_b) is set equal to the parameterization of the observed $\Upsilon(2S)$ p_T spectrum. Left: distribution of the transverse momentum of the dimuon. Right: distribution of the transverse energy of the photon.

We believe the event in which the χ_{b1} and χ_{b2} are produced with different p_T spectra is unlikely, because it would imply that different production mechanisms are at play. To test this hypothesis, we use the same procedure outlined above, but define two signal regions, one around the peak of the χ_{b1} and one around the peak of the χ_{b2}. Figure 3.9 shows the comparisons of the background-subtracted p_T (χ_b), $y(\Upsilon)$, p_T (Υ) and $E_T(\gamma)$ spectra for the χ_{b1} and the χ_{b2}. Since the data shows no evidence, within statistical uncertainties, that the χ_{b1} and χ_{b2} are produced with different spectra and the data and Monte Carlo agreement is best when the two resonances are produced using the measured $\Upsilon(2S)$ production spectra, we take this as our default scenario to derive the ratio of efficiencies $\varepsilon_1/\varepsilon_2$.

3.9 RESULTS AND DISCUSSION

The results of the measurement of the ratio R_p and of the ratio of the χ_{b2} to χ_{b1} production cross sections for the kinematic range $|y(\Upsilon)| < 1.25$, $|\eta(\gamma)| < 1.0$ are reported in Tables 3.10 and 3.11, respectively, for different ranges of p_T (Υ). The first uncertainty is statistical, the second is systematic, and the third comes

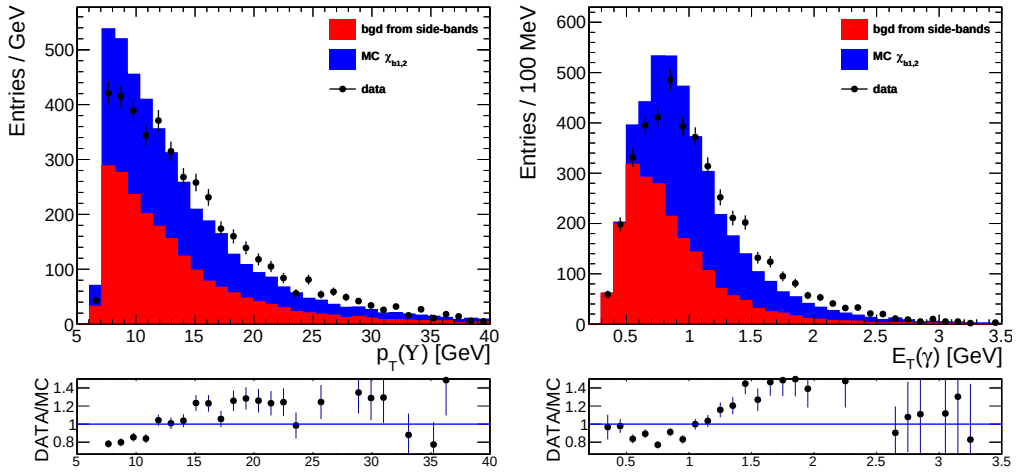

Figure 3.8.: Comparison of Monte Carlo and data spectra when the input p_T (χ_b) is set equal to the parameterization of the observed $\Upsilon(1S)$ p_T spectrum. Left: distribution of the transverse momentum of the dimuon. Right: distribution of the transverse energy of the photon.

from the uncertainty on the branching fractions in the measurement of the cross section ratio. Separate columns are dedicated to the uncertainty derived from the extreme polarization scenarios in the helicity and Collins–Soper frames, by choosing from Tables 3.8 and 3.7 the scenarios that give the largest variations relative to the unpolarized case.

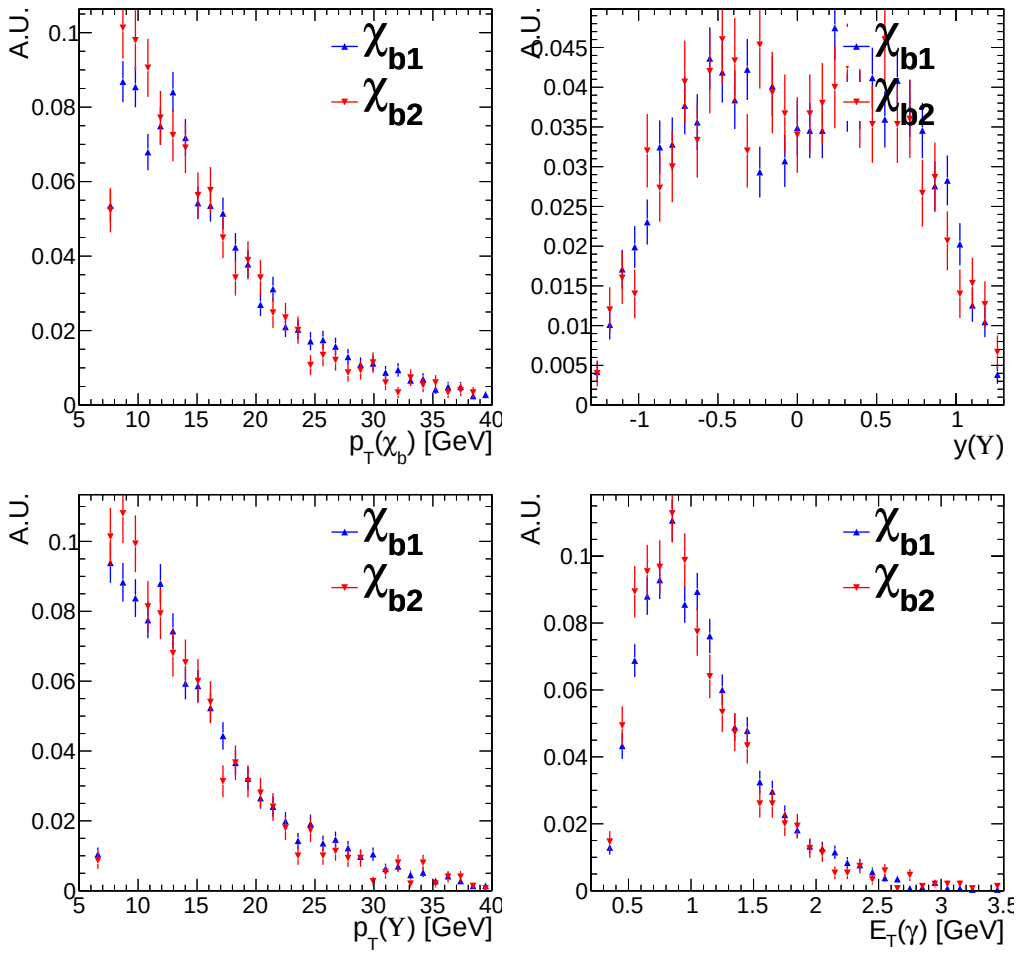

Figure 3.9.: Comparison of background-subtracted p_T (χ_b) (top left), y(Υ) (top right) p_T (Υ) (bottom left) and $E_T(\gamma)$ (bottom right) spectra for candidates in the χ_{b1} and in the χ_{b2} signal regions.

Table 3.10.: Measurements of $\sigma(\chi_{b2})/\sigma(\chi_{b1})$ for the given $p_T(\Upsilon)$ ranges derived using the branching fractions from Ref. [6], assuming unpolarized χ_b production. The first uncertainty is statistical, the second is systematic, and the third from the branching fraction uncertainties. The last two columns report the uncertainties derived from the extreme polarization scenarios in the helicity (HX) and Collins–Soper (CS) frames.

$p_T(\Upsilon)$ [GeV]	$\sigma(\chi_{b2})/\sigma(\chi_{b1})$	HX	CS
7 - 11	1.14 ± 0.20 (stat.) ± 0.06 (syst.) ± 0.10 (BR)	$^{+0.25}_{-0.24}$	$^{+0.04}_{-0.05}$
11 - 16	0.866 ± 0.106 (stat.) ± 0.048 (syst.) ± 0.078 (BR)	$^{+0.175}_{-0.184}$	$^{+0.024}_{-0.010}$
16 - 20	0.97 ± 0.14 (stat.) ± 0.07 (syst.) ± 0.09 (BR)	$^{+0.16}_{-0.18}$	$^{+0.03}_{-0.02}$
20 - 40	1.06 ± 0.13 (stat.) ± 0.06 (syst.) ± 0.10 (BR)	$^{+0.17}_{-0.18}$	$^{+0.08}_{-0.05}$

Table 3.11.: Measurements of $\frac{\sigma(\chi_{b2})\mathcal{B}(\chi_{b2})}{\sigma(\chi_{b1})\mathcal{B}(\chi_{b1})}$ for the given $p_T(\Upsilon)$ ranges derived assuming unpolarized χ_b production. The first uncertainty is statistical, the second is systematic, and the third from the branching fraction uncertainties. The last two columns report the uncertainties derived from the extreme polarization scenarios in the helicity (HX) and Collins–Soper (CS) frames.

$p_T(\Upsilon)$ [GeV]	$\frac{\sigma(\chi_{b2})\mathcal{B}(\chi_{b2})}{\sigma(\chi_{b1})\mathcal{B}(\chi_{b1})}$	HX	CS
7 - 11	0.64 ± 0.11 (stat.) ± 0.03 (syst.)	$^{+0.14}_{-0.14}$	$^{+0.03}_{-0.03}$
11 - 16	0.488 ± 0.060 (stat.) ± 0.027 (syst.)	$^{+0.099}_{-0.103}$	$^{+0.013}_{-0.005}$
16 - 20	0.55 ± 0.08 (stat.) ± 0.04 (syst.)	$^{+0.09}_{-0.10}$	$^{+0.02}_{-0.01}$
20 - 40	0.60 ± 0.07 (stat.) ± 0.04 (syst.)	$^{+0.09}_{-0.10}$	$^{+0.05}_{-0.03}$

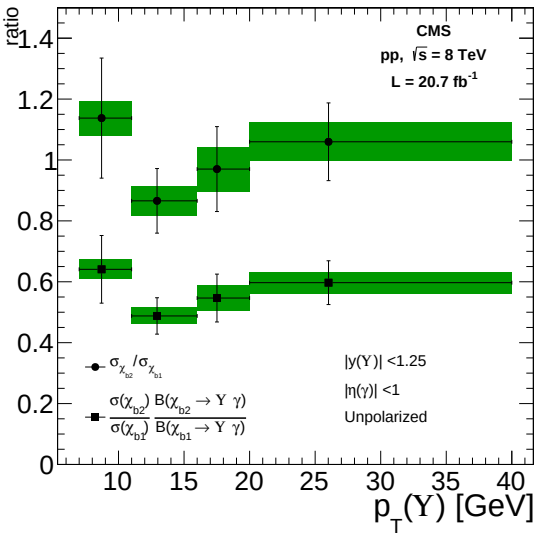

Figure 3.10.: Ratio of the χ_{b2} to χ_{b1} production cross sections (circles) and ratio of the cross sections times the branching fractions to $\Upsilon(1S) + \gamma$ (squares) as a function of the Υ transverse momentum with the hypothesis of unpolarized production. The error bars correspond to the statistical uncertainties and the green band corresponds to the systematic uncertainties. For the cross section ratios,

CONCLUSIONS

In this thesis is presented the measurement of the ratio

$$\mathcal{R} \equiv \frac{\sigma(pp \to \chi_{b2} + X)\mathcal{B}(\chi_{b2} \to \Upsilon(1S) + \gamma)}{\sigma(pp \to \chi_{b1} + X)\mathcal{B}(\chi_{b1} \to \Upsilon(1S) + \gamma)}$$

as a function of the Υ transverse momentum up to $p_T(\Upsilon) = 40\,\text{GeV}$ for the kinematic range $|y(J/\psi)| < 1.0$, $|\eta(\gamma)| < 1.0$ in pp collisions at $\sqrt{s} = 8\,\text{TeV}$ with a data sample corresponding to an integrated luminosity of 20.7fb^{-1}. The corresponding values for the ratio of the χ_{b2} to χ_{b1} production cross sections have been determined, the results are reported in tables 3.10 and 3.11 respectively and summarized in figure 3.10.

The effect of several different χ_b polarization scenarios on the photon reconstruction efficiency has been investigated and correction factors provided to transport the result to any polarization scenario. This is the first measurement of the χ_b production cross section ratio made in hadron collisions. These measurements can provide important input to and constraints on future theoretical calculations of quarkonium production. For example this measure rules out the results obtained with spin counting predicted by the Color Evaporation Model while it is in agreement within the experimental errors with the prediction of [27].

A FIT RESULTS FOR ALTERNATIVE CHOICES OF FITTING FUNCTIONS

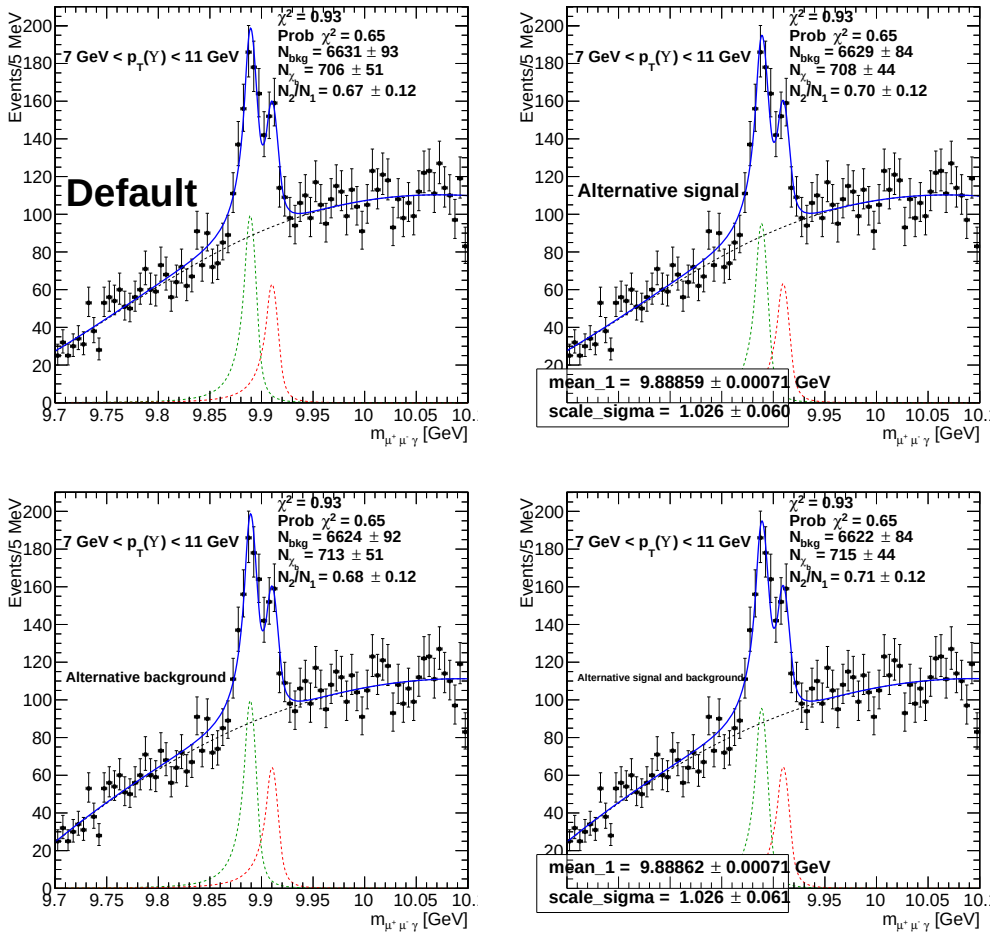

Figure A.1.: Fits to signal and background for several alternative fitting strategies $7\ \text{GeV} < p_T(\Upsilon) < 11\ \text{GeV}$

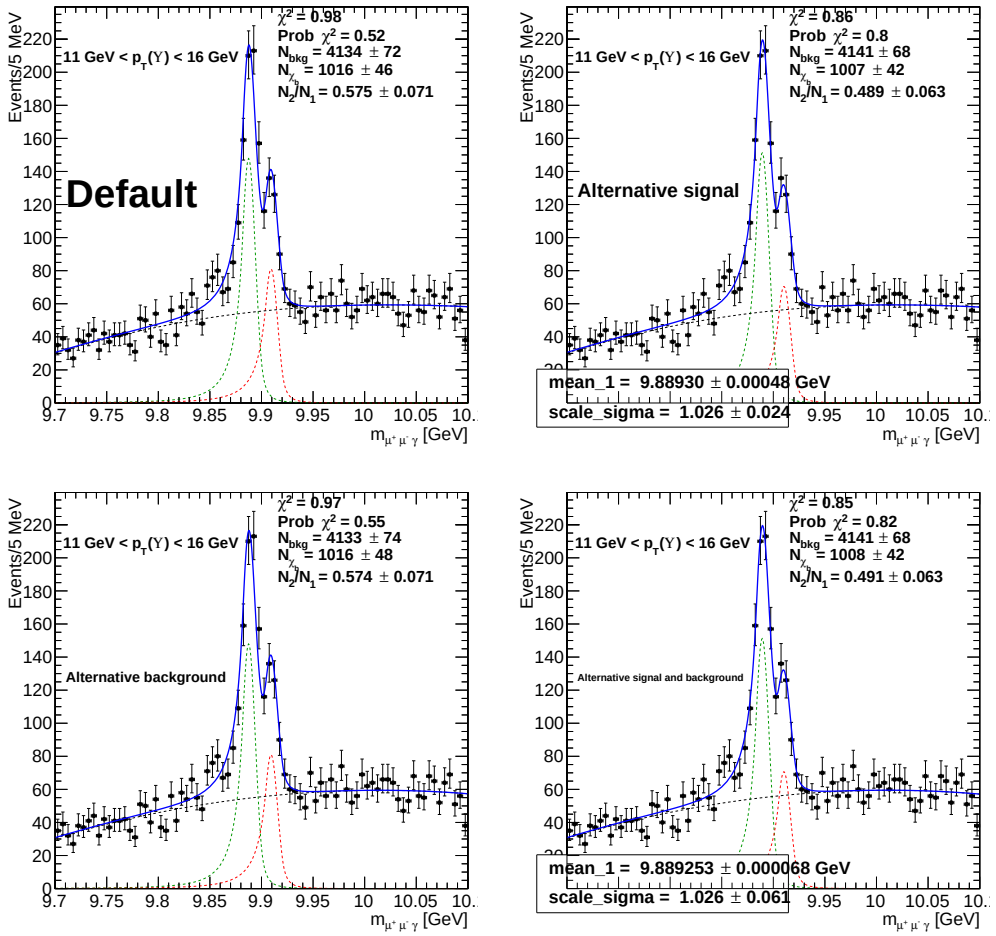

Figure A.2.: Fits to signal and background for several alternative fitting strategies 11 GeV $<$ $p_T(\Upsilon) < 16$ GeV

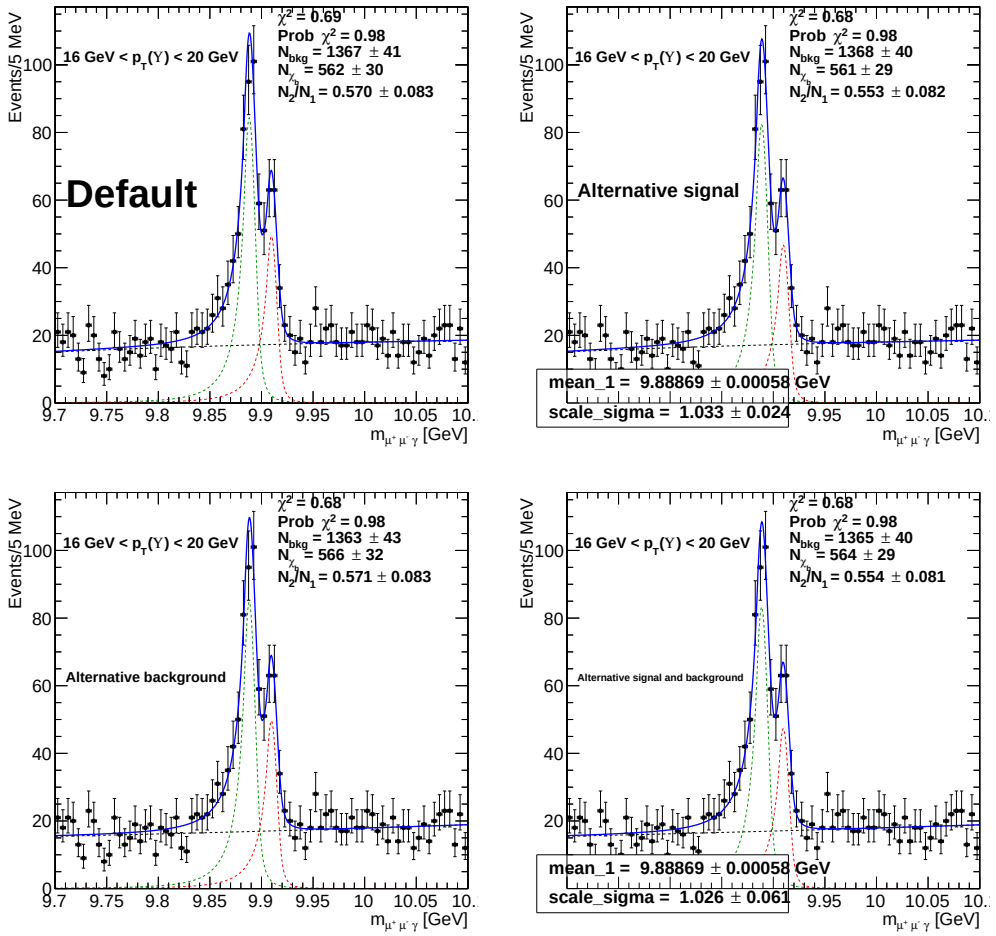

Figure A.3.: Fits to signal and background for several alternative fitting strategies 16 GeV $<$ $p_T(\Upsilon) < 20$ GeV

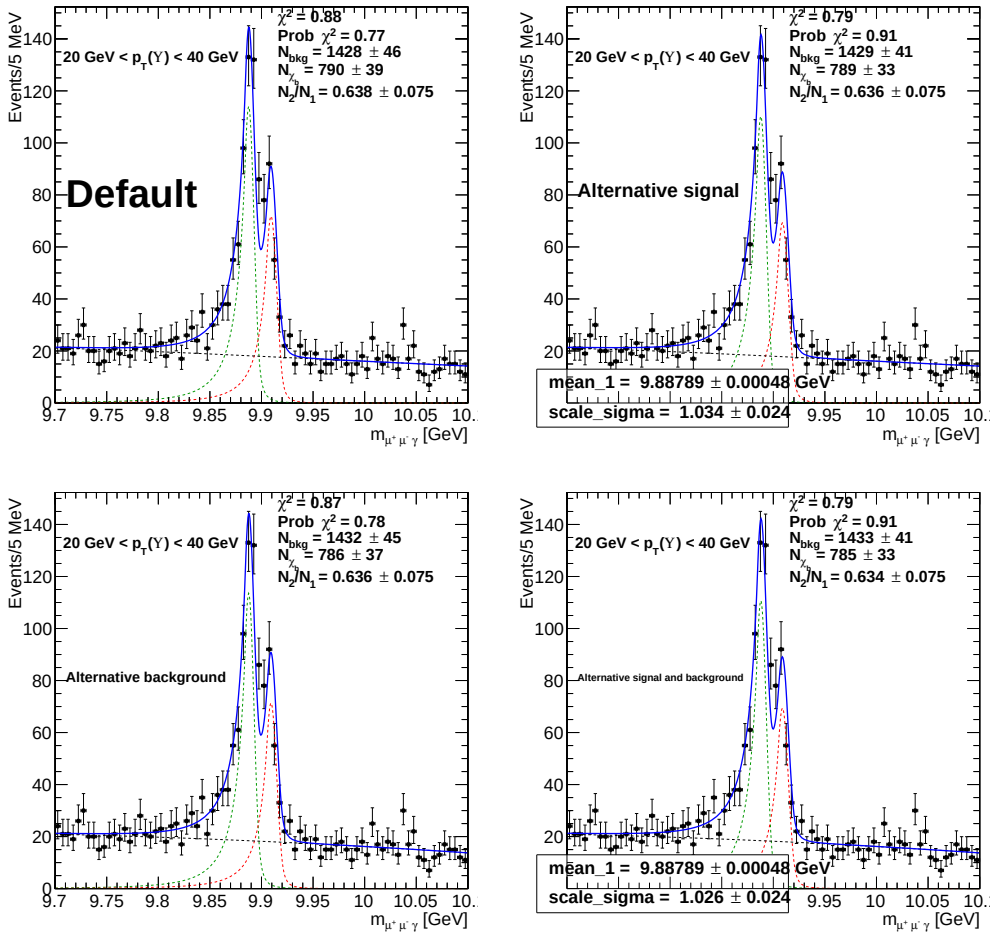

Figure A.4.: Fits to signal and background for several alternative fitting strategies 20 GeV $<$ $p_T(\Upsilon) < 40$ GeV

B UNCERTAINTIES IN EFFICIENCY CALCULATIONS WITH WEIGHTS

For evaluating the efficiency of a selection, Monte Carlo simulations are often used. The distribution of the events in the phase space must be assumed but, as this is crucial in determining the efficiency, if another distribution must be considered two solutions arise: to produce another simulation starting from the different distribution, or reweight each event of the simulation with the ratio of the probabilities of that event to happen in that specific a point of the phase space. In this appendix we derive how to compute the statistical uncertainties associated to efficiencies when these are evaluated from reweighted simulations.

B.1 ASSUMPTIONS AND NOTATION

We assume the phase space to be divided in N_{bins} bins. In a simulation with N events the distribution of the *generated events* in the bins (N_i) follows a *multinomial distribution* with probabilities $\mathcal{E}_i$ so that, with a large sample, $N_i \sim N \cdot \mathcal{E}_i$. Also the distribution of *selected events* in the bins (n_i) follows the same distribution but with probabilities ε_i so that, with a large sample, $n_i \sim N \cdot \varepsilon_i$. As we will consider different sets of weights and the uncertainties on the ratio of efficiencies obtained reweighting the same simulation with different sets of weights, we will denote a set of weights with a Greek letter; α_i and β_i will thus be the weights associated to the i-th bin in two different sets of weights. We will then define

$$N_\alpha = \sum_{i=1}^{N_{bins}} N_i \alpha_i \qquad \text{and} \qquad n_\alpha = \sum_{i=1}^{N_{bins}} n_i \alpha_i \tag{B.1}$$

In the limit of an infinite number of bins, each bin contains at most one generated event so that, summing only over the bins which contain a generated event,

$$N_\alpha = \sum_{i=1}^{N} \alpha_i \qquad \text{and} \qquad n_\alpha = \sum_{i=1}^{N} \mathcal{A}_i \alpha_i \tag{B.2}$$

where $\mathcal{A}_i$ is the efficiency factor:

$$\mathcal{A}_i = \begin{cases} 1 & \text{if the event } i \text{ is selected,} \\ 0 & \text{if the event } i \text{ is not selected.} \end{cases}$$

The efficiency without reweighting is denoted by $\varepsilon = n/N$ and the efficiency computed reweighting the simulation with the set of weights α is denoted with $\varepsilon_\alpha = n_\alpha/N_\alpha$. Weights are assumed to be perfectly known i.e. with zero uncertainty.

B.2 VARIANCES RELEVANT TO THE PROBLEM

The covariance of a multinomial distribution is

$$V(N_i, N_j) = N(\mathcal{E}_i\delta_{ij} - \mathcal{E}_i\mathcal{E}_j) \tag{B.3}$$

similarly

$$V(n_i, n_j) = N(\varepsilon_i\delta_{ij} - \varepsilon_i\varepsilon_j) \tag{B.4}$$

while, using the linearity of covariances,

$$V(n_i, N_j) = V(n_i, n_j) + V(n_i, N_j - n_j)$$

as n_i and $N_j - n_j$ corresponds to disjoint samples, from (B.4) follows

$$V(n_i, N_j - n_j) = -N\varepsilon_i(\mathcal{E}_j - \varepsilon_j)$$

where $\mathcal{E}_j - \varepsilon_j$, is the probability of the generated event to be in the j-th bin but not be selected. Using (B.4) then follows

$$V(n_i, N_j) = N(\varepsilon_i\delta_{ij} - \varepsilon_i\mathcal{E}_j). \tag{B.5}$$

From the definition of N_α (B.1) follows that its variance is

$$\begin{aligned} V(N_\alpha, N_\alpha) &= \sum_{i=1}^{N_{bins}} \sum_{j=1}^{N_{bins}} V(N_i, N_j)\alpha_i\alpha_j \\ &= N \sum_{i=1}^{N_{bins}} \sum_{j=1}^{N_{bins}} (\mathcal{E}_i\delta_{ij} - \mathcal{E}_i\mathcal{E}_j)\alpha_i\alpha_j \end{aligned}$$

similarly the covariance between N_α and N_β will be

$$\begin{aligned} V(N_\alpha, N_\beta) &= \sum_{i=1}^{N_{bins}} \sum_{j=1}^{N_{bins}} V(N_i, N_j)\alpha_i\beta_j \\ &= N \sum_{i=1}^{N_{bins}} \sum_{j=1}^{N_{bins}} (\mathcal{E}_i\delta_{ij} - \mathcal{E}_i\mathcal{E}_j)\alpha_i\beta_j \end{aligned}$$

Substituting $N\mathcal{E}_i$ by N_i we can obtain an estimate of $V(N_\alpha, N_\alpha)$ and $V(N_\alpha, N_\beta)$:

$$V(N_\alpha, N_\alpha) = \sum_{i=1}^{N_{bins}} N_i(\alpha_i)^2 - \frac{1}{N}\left(\sum_{i=1}^{N_{bins}} N_i\alpha_i\right)^2$$
$$V(N_\alpha, N_\beta) = \sum_{i=1}^{N_{bins}} N_i\alpha_i\beta_i - \frac{1}{N}\left(\sum_{i=1}^{N_{bins}} N_i\alpha_i\right)\left(\sum_{i=1}^{N_{bins}} N_i\beta_i\right)$$

and in the infinite bins limit:

$$V(N_\alpha, N_\alpha) = \sum_{i=1}^{N} (\alpha_i)^2 - \frac{1}{N}\left(\sum_{i=1}^{N} \alpha_i\right)^2$$
$$V(N_\alpha, N_\beta) = \sum_{i=1}^{N} \alpha_i\beta_i - \frac{1}{N}\left(\sum_{i=1}^{N} \alpha_i\right)\left(\sum_{i=1}^{N} \beta_i\right).$$

Similarly

$$V(n_\alpha, n_\alpha) = \sum_{i=1}^{N_{bins}} n_i(\alpha_i)^2 - \frac{1}{N}\left(\sum_{i=1}^{N_{bins}} n_i\alpha_i\right)^2 = \sum_{i=1}^{N} \mathcal{A}_i(\alpha_i)^2 - \frac{1}{N}\left(\sum_{i=1}^{N} \mathcal{A}_i\alpha_i\right)^2$$
$$V(n_\alpha, n_\beta) = \sum_{i=1}^{N_{bins}} n_i\alpha_i\beta_i - \frac{1}{N}\left(\sum_{i=1}^{N_{bins}} n_i\alpha_i\right)\left(\sum_{i=1}^{N_{bins}} n_i\beta_i\right) =$$
$$= \sum_{i=1}^{N} \mathcal{A}_i\alpha_i\beta_i - \frac{1}{N}\left(\sum_{i=1}^{N} \mathcal{A}_i\alpha_i\right)\left(\sum_{i=1}^{N} \mathcal{A}_i\beta_i\right).$$

To compute $V(n_\alpha, N_\alpha)$ and $V(n_\alpha, N_\beta)$, starting from (B.5) we obtain:

$$V(n_\alpha, N_\alpha) = \sum_{i=1}^{N_{bins}} n_i(\alpha_i)^2 - \frac{1}{N}\left(\sum_{i=1}^{N_{bins}} n_i\alpha_i\right)\left(\sum_{i=1}^{N_{bins}} N_i\alpha_i\right) =$$
$$= \sum_{i=1}^{N} \mathcal{A}_i(\alpha_i)^2 - \frac{1}{N}\left(\sum_{i=1}^{N} \mathcal{A}_i\alpha_i\right)\left(\sum_{i=1}^{N} \alpha_i\right)$$
$$V(n_\alpha, N_\beta) = \sum_{i=1}^{N_{bins}} n_i\alpha_i\beta_i - \frac{1}{N}\left(\sum_{i=1}^{N_{bins}} n_i\alpha_i\right)\left(\sum_{i=1}^{N_{bins}} N_i\beta_i\right) =$$
$$= \sum_{i=1}^{N} \mathcal{A}_i\alpha_i\beta_i - \frac{1}{N}\left(\sum_{i=1}^{N} \mathcal{A}_i\alpha_i\right)\left(\sum_{i=1}^{N} \beta_i\right).$$

B.3 ERROR PROPAGATION

From error propagation it follows that the variance of a variable having expression

$$f = \frac{\prod_{i=1}^{n_a} a_i}{\prod_{k=1}^{n_b} b_k}$$

is

$$\frac{V(f,f)}{f^2} = \sum_{i=1}^{n_a} \frac{V(a_i,a_i)}{a_i^2} + \sum_{k=1}^{n_b} \frac{V(b_k,b_k)}{b_k^2} - 2\sum_{i=1}^{n_a}\sum_{k=1}^{n_b} \frac{V(a_i,b_k)}{a_i b_k} + 2\sum_{i=1}^{n_a}\sum_{j=i+1}^{n_a} \frac{V(a_i,a_j)}{a_i a_j} + 2\sum_{k=1}^{n_b}\sum_{l=k+1}^{n_b} \frac{V(b_k,b_l)}{b_k b_l}. \quad \text{(B.6)}$$

B.3.1 Uncertainty on efficiency

The efficiency computed reweighting the simulation is defined as $\varepsilon_\alpha = n_\alpha/N_\alpha$, from (B.6) its associated error is

$$\frac{V(\varepsilon_\alpha,\varepsilon_\alpha)}{\varepsilon_\alpha^2} = \frac{V(n_\alpha,n_\alpha)}{n_\alpha^2} + \frac{V(N_\alpha,N_\alpha)}{N_\alpha^2} - 2\frac{V(n_\alpha,N_\alpha)}{n_\alpha N_\alpha}$$

Substituting the covariances with the ones obtained in section B.2:

$$\begin{aligned} V(\varepsilon_\alpha,\varepsilon_\alpha) = {} & \frac{1}{N_\alpha^2}\left[\sum_{i=1}^{N} \mathcal{A}_i(\alpha_i)^2 - \frac{1}{N}\left(\sum_{i=1}^{N} \mathcal{A}_i\alpha_i\right)^2\right] + \\ & + \frac{n_\alpha^2}{N_\alpha^4}\left[\sum_{i=1}^{N} (\alpha_i)^2 - \frac{1}{N}\left(\sum_{i=1}^{N} \alpha_i\right)^2\right] + \\ & - 2\frac{n_\alpha}{N_\alpha^3}\left[\sum_{i=1}^{N} \mathcal{A}_i(\alpha_i)^2 - \frac{1}{N}\left(\sum_{i=1}^{N} \mathcal{A}_i\alpha_i\right)\left(\sum_{i=1}^{N} \alpha_i\right)\right] \end{aligned} \quad \text{(B.7)}$$

Note that in the no reweighting limit ($\alpha_i = 1$)

$$\begin{cases} N_\alpha & \to N \\ \sum_{i=1}^{N}(\alpha_i)^2 = \sum_{i=1}^{N} \alpha_i & \to N \\ \sum_{i=1}^{N} \mathcal{A}_i(\alpha_i)^2 = \sum_{i=1}^{N} \mathcal{A}_i\alpha_i & \to n \end{cases}$$

the last two terms of (B.7) vanish and the first term becomes

$$\frac{\varepsilon(1-\varepsilon)}{N}$$

recovering the well known expression for the variance of the binomial distribution.

B.4 RATIO OF EFFICIENCIES

The ratio of two efficiencies computed reweighting the same simulation but with different sets of weights is:

$$\frac{\varepsilon_\alpha}{\varepsilon_\beta} = \frac{n_\alpha}{N_\alpha} \cdot \frac{N_\beta}{n_\beta}$$

its variance, from equation (B.6) is:

$$\frac{V\left(\frac{\varepsilon_\alpha}{\varepsilon_\beta}, \frac{\varepsilon_\alpha}{\varepsilon_\beta}\right)}{\left(\frac{\varepsilon_\alpha}{\varepsilon_\beta}\right)^2} = \frac{V(\varepsilon_\alpha, \varepsilon_\alpha)}{\varepsilon_\alpha^2} + \frac{V(\varepsilon_\beta, \varepsilon_\beta)}{\varepsilon_\beta^2} - 2\frac{V(\varepsilon_\alpha, \varepsilon_\beta)}{\varepsilon_\alpha \varepsilon_\beta}$$

where

$$\frac{V(\varepsilon_\alpha, \varepsilon_\beta)}{\varepsilon_\alpha \varepsilon_\beta} = \frac{V(n_\alpha, n_\beta)}{n_\alpha n_\beta} + \frac{V(N_\alpha, N_\beta)}{N_\alpha N_\beta} - \frac{V(n_\alpha, N_\beta)}{n_\alpha N_\beta} - \frac{V(n_\beta, N_\alpha)}{n_\beta N_\alpha}$$

B.5 UNCERTAINTY ON $\varepsilon_1/\varepsilon_2$

In chapter 3 the ratio $\varepsilon_1/\varepsilon_2$ and its associated statistical uncertainty are computed in different polarization scenarios with a reweighting of the simulation. As for computing the two efficiencies different simulations have been used, it is assumed $V(\varepsilon_1, \varepsilon_2)$ to be zero so that

$$\frac{V\left(\frac{\varepsilon_1}{\varepsilon_2}, \frac{\varepsilon_1}{\varepsilon_2}\right)}{\left(\frac{\varepsilon_1}{\varepsilon_2}\right)^2} = \frac{V(\varepsilon_1, \varepsilon_1)}{\varepsilon_1^2} + \frac{V(\varepsilon_2, \varepsilon_2)}{\varepsilon_2^2}$$

Similarly when computing the ratio of the ratios between the polarized and the unpolarized case: $\frac{\varepsilon_{1,\mathrm{pol}}}{\varepsilon_{2,\mathrm{pol}}} / \frac{\varepsilon_{1,\mathrm{unpol}}}{\varepsilon_{2,\mathrm{unpol}}}$, the uncertainty is computed:

$$\frac{V\left(\frac{\varepsilon_{1,\mathrm{pol}}}{\varepsilon_{2,\mathrm{pol}}} / \frac{\varepsilon_{1,\mathrm{unpol}}}{\varepsilon_{2,\mathrm{unpol}}}, \frac{\varepsilon_{1,\mathrm{pol}}}{\varepsilon_{2,\mathrm{pol}}} / \frac{\varepsilon_{1,\mathrm{unpol}}}{\varepsilon_{2,\mathrm{unpol}}}\right)}{\left(\frac{\varepsilon_{1,\mathrm{pol}}}{\varepsilon_{2,\mathrm{pol}}} / \frac{\varepsilon_{1,\mathrm{unpol}}}{\varepsilon_{2,\mathrm{unpol}}}\right)^2} = \frac{V\left(\frac{\varepsilon_{1,\mathrm{pol}}}{\varepsilon_{1,\mathrm{unpol}}}, \frac{\varepsilon_{1,\mathrm{pol}}}{\varepsilon_{1,\mathrm{unpol}}}\right)}{\left(\frac{\varepsilon_{1,\mathrm{pol}}}{\varepsilon_{1,\mathrm{unpol}}}\right)^2} + \frac{V\left(\frac{\varepsilon_{2,\mathrm{pol}}}{\varepsilon_{2,\mathrm{unpol}}}, \frac{\varepsilon_{2,\mathrm{pol}}}{\varepsilon_{2,\mathrm{unpol}}}\right)}{\left(\frac{\varepsilon_{2,\mathrm{pol}}}{\varepsilon_{2,\mathrm{unpol}}}\right)^2}.$$

BIBLIOGRAPHY

[1] R Aaij et al. Measurement of the cross-section ratio $\sigma(\chi_{c2})/\sigma(\chi_{c1})$ for prompt χ_c production at $\sqrt{s} = 7$ TeV. *Phys.Lett.*, B714:215–223, 2012.

[2] A. et al. Abulencia. Measurement of $\sigma_{\chi_{c2}}\lfloor(\chi_{c2} \to j/\psi\gamma)/\sigma_{\chi_{c1}}\lfloor(\chi_{c1} \to j/\psi\gamma)$ in $p\overline{p}$ collisions at $\sqrt{s} = 1.96$ tev. *Phys. Rev. Lett.*, 98(23):232001, Jun 2007.

[3] G. Acquistapace et al. CMS, the magnet project: Technical design report. *CERN-LHCC-97-10*, 1997.

[4] I. Vasileva Akin, S. Argirò, T. Dahms, D. Giordano, and E. Usai. Measurement of the ratio $\sigma(pp \to \chi_{b2} + X)/\sigma(pp \to \chi_{b1} + X)$ from radiative decays in $J/\psi + \gamma$ using converted photons. Technical Report AN-2011/332, 2011.

[5] M. Benedikt, P. Collier, V. Mertens, J. Poole, and K. Schindl. LHC Design Report. 3. The LHC injector chain. *CERN-2004-003-V-3, CERN-2004-003*, 2004.

[6] J. Beringer et al. Review of particle physics. *Phys. Rev. D*, 86:010001, 2012.

[7] Oliver S. Bruning, P. Collier, P. Lebrun, S. Myers, R. Ostojic, et al. LHC Design Report. 1. The LHC Main Ring. *CERN-2004-003-V-1, CERN-2004-003*, 2004.

[8] O. Buning, P. Collier, P. Lebrun, S. Myers, R. Ostojic, et al. LHC Design Report. 2. The LHC infrastructure and general services. *CERN-2004-003-V-2, CERN-2004-003*, 2004.

[9] S. Chatrchyan et al. The CMS experiment at the CERN LHC. *JINST*, 3:S08004, 2008.

[10] Serguei Chatrchyan et al. Measurement of the relative prompt production rate of chi(c2) and chi(c1) in pp collisions at $\sqrt{s} = 7$ TeV. *Eur.Phys.J.*, C72:2251, 2012.

[11] Serguei Chatrchyan et al. Measurement of the Y(1S), Y(2S), and Y(3S) cross sections in pp collisions at $\sqrt{s} = 7$ TeV. 2013.

[12] Serguei Chatrchyan et al. Measurement of the Y1S, Y2S and Y3S polarizations in pp collisions at $\sqrt{s} = 7$ TeV. *Phys.Rev.Lett.*, 110:081802, 2013.

[13] CDF Collaboration. Production of J/ψ mesons from χ_c meson decays in $p\bar{p}$ collisions at $\sqrt{s} = 1.8$ tev. *Phys. Rev. Lett.*, 1997.

[14] CDF Collaboration. Measurement of $\sigma(\chi(c2)B(\chi(c2) \to J/\psi))/\sigma(\chi(c1)B(\chi(c1) \to J/\psi))$ in p anti-p collisions at $\sqrt{s} = 1.96$ tev. *Phys. Rev. Lett.*, 2007.

[15] CMS Collaboration. CMS, the Compact Muon Solenoid. Muon technical design report. *CERN-LHCC-97-32*, 1997.

[16] CMS Collaboration. CMS: The electromagnetic calorimeter. Technical design report. *CERN-LHCC-97-33, CMS-TDR-4*, 1997.

[17] CMS Collaboration. CMS, tracker technical design report. *CERN-LHCC-98-06, CMS-TDR-5*, 1998.

[18] CMS Collaboration. Measurement of relative prompt production rate of χ_{c2} and χ_{c1} in pp collisions at $\sqrt{s} = 7$ tev. *European Physical Juornal C*, 2012.

[19] LHCb Collaboration. Measurement of the cross section ratio $\sigma(\chi(c2)/\sigma(\chi(c1)$ for prompt χ_c production at $\sqrt{s} = 7$. *Phis. Lett. B*, 2012.

[20] John C. Collins and Davison E. Soper. Angular Distribution of Dileptons in High-Energy Hadron Collisions. *Phys. Rev. D*, 16:2219, 1977.

[21] Kaplan David. Effective field theories. *Lectures given at the Seventh Summer School in Nuclear Physics, Seattle*, 1995.

[22] Braaten Eric. Introduction to the NRQCD factorization approach to heavy quarkonium. *arXiv:hep-ph/9702225*, 1997.

[23] Pietro Faccioli, Carlos Lourenço, Joao Seixas, and Hermine K. Wöhri. Determination of χ_c and χ_b polarizations from dilepton angular distributions in radiative decays. *Phys. Rev. D*, 83:096001, 2011.

[24] Bodwin G.T., Braaten E., and Lepage G.P. Rigorous QCD analysis of inclusive annihilation and production of heavy quarkonium. *Phys. Rev.*, 1995.

[25] Polchinski Joseph. Effective field theories and the fermi surface. *Lectures presented at TASI*, 1992.

[26] Vardan Khachatryan et al. CMS Tracking Performance Results from early LHC Operation. *Eur.Phys.J.*, C70:1165–1192, 2010.

[27] A. K. Likhoded, A. V. Luchinsky, and S. V. Poslavsky. Production of χ_b mesons at the LHC. *Phys. Rev. D*, 86:074027, Oct 2012.

[28] Yan-Qing Ma, Kai Wang, and Kuang-Ta Chao. Qcd radiative corrections to χ_{cJ} production at hadron colliders. *Phys. Rev. D*, 83:111503, Jun 2011.

[29] M. J. Oreglia. *A study of the reactions* $\psi' \to \gamma\gamma\psi$. PhD thesis, Stanford University, 1980. SLAC Report SLAC-R-236.

[30] The Atlas Collaboration. Observation of a new χ_b state in radiative transitions of $\upsilon(1s)$ and $\upsilon(2s)$ at atlas. *CERN-PH-EP-2011-225*, 2011.

[31] W. Verkerke and D. Kirkby. The roofit toolkit for data modeling.